

Molecular gas in submillimetre-faint, star-forming ultraluminous galaxies at $z > 1$

C. M. Casey,^{1,2*}† S. C. Chapman,¹ R. Neri,³ F. Bertoldi,⁴ I. Smail,⁵ K. Coppin,^{5,6}
T. R. Greve,⁷ M. S. Bothwell,¹ R. J. Beswick,⁸ A. W. Blain,⁹ P. Cox,³ R. Genzel,¹⁰
T. W. B. Muxlow,⁷ A. Omont¹¹ and A. M. Swinbank⁵

¹*Institute of Astronomy, Madingley Road, Cambridge CB3 0HA*

²*Institute for Astronomy, University of Hawaii, 2680 Woodlawn Dr, Honolulu, HI 96822, USA*

³*Institut de Radio Astronomie Millimetrique (IRAM), St. Martin d’Heres, France*

⁴*Argenlander Institute for Astronomy, University of Bonn, Auf dem Hügel 71, 53121 Bonn, Germany*

⁵*Institute for Computational Cosmology, Durham University, South Road, Durham DH1 3LE*

⁶*McGill University, 3600 rue University, Montreal, QC, H3A 2T8, Canada*

⁷*Dark Cosmology Centre, Niels Bohr Institute, University of Copenhagen, Juliane Maries Vej 30, DK-2100 Copenhagen, Denmark*

⁸*Jodrell Bank Observatory, University of Manchester, Macclesfield SK11 9DL*

⁹*Department of Physics & Astronomy, University of Leicester, University Road, Leicester LE1 7RH*

¹⁰*MPE, Giessenbachstrasse 1, D-85741 Garching, Germany*

¹¹*Institut d’Astrophysique de Paris, CNRS and Université Pierre et Marie Curie, 98 Bis Boulevard Arago, 75014 Paris, France*

Accepted 2011 April 9. Received 2011 April 9; in original form 2009 October 31

ABSTRACT

We present interferometric CO observations of 12 $z \sim 2$ submillimetre-faint, star-forming radio galaxies (SFRGs) which are thought to be ultraluminous infrared galaxies (ULIRGs) possibly dominated by warmer dust ($T_{\text{dust}} \gtrsim 40$ K) than submillimetre galaxies (SMGs) of similar luminosities. Four other CO-observed SFRGs are included from the literature, and all the observations are taken at the Plateau de Bure Interferometer (PdBI) in the compact configuration. 10 of the 16 SFRGs observed in CO (63 per cent) are detected at $>4\sigma$ with a mean inferred molecular gas mass of $\sim 2 \times 10^{10} M_{\odot}$. SFRGs trend slightly above the local ULIRG $L_{\text{FIR}}-L'_{\text{CO}}$ relation. Since SFRGs are about two times fainter in radio luminosity but exhibit similar CO luminosities to SMGs, this suggests SFRGs are slightly more efficient star formers than SMGs at the same redshifts. SFRGs also have a narrow mean CO linewidth, $320 \pm 80 \text{ km s}^{-1}$. Many SMGs have similarly narrow CO linewidths, but very broad features ($\sim 900 \text{ km s}^{-1}$) are present in a few SMGs and are absent from SFRGs. SFRGs bridge the gap between properties of very luminous $>5 \times 10^{12} L_{\odot}$ SMGs and those of local ULIRGs, and are consistent with intermediate-stage major mergers. We suspect that more moderate luminosity SMGs, not yet surveyed in CO, would show similar molecular gas properties to SFRGs. The active galactic nucleus (AGN) fraction of SFRGs is consistent with SMGs and is estimated to be 0.3 ± 0.1 , suggesting that SFRGs are observed near the peak phase of star formation activity and not in a later, post-SMG enhanced AGN phase. The excitation analysis of one SFRG is consistent with the CO excitation observed in SMGs [turning over beyond $^{12}\text{CO}(J = 4 \rightarrow 3)$]. This CO survey of SFRGs serves as a pilot project for the much more extensive survey of *Herschel* and SCUBA-2 selected sources which only partially overlap with SMGs. Better constraints on the CO properties of a diverse high- z ULIRG population are needed from ALMA to determine the evolutionary origin of extreme starbursts, and what role ULIRGs serve in catalyzing the formation of massive stellar systems in the early Universe.

Key words: galaxies: evolution – galaxies: high-redshift – galaxies: starburst.

1 INTRODUCTION

Ultraluminous infrared galaxies (ULIRGs) exhibit some of the most extreme star formation rates in the Universe. The volume density of

*Hubble Fellow.

†E-mail: cmcasey@ifa.hawaii.edu

higher redshift ULIRGs peaks at $z \sim 2-3$ (Chapman et al. 2005) – this is also the peak epoch in the cosmic star formation rate density and volume density of active galactic nucleus (AGN; e.g. Fan et al. 2001; Richards et al. 2006). Not only does this indicate a possible link between supermassive black hole growth and rapid star formation, but it also signals the most active phase in galaxy evolution and formation. ULIRGs exhibit very intense ($\text{SFR} \gtrsim 200 M_{\odot} \text{ yr}^{-1}$), short-lived bursts ($\tau \sim 100 \text{ Myr}$) of star formation. The possible life cycle of a ULIRG, from star formation dominated, dust-enshrouded galaxy, to obscured AGN and then luminous quasar (e.g. Sanders et al. 1988; Veilleux et al. 2009), provides a testable evolutionary sequence.

The best studied ULIRGs at high redshift are submillimetre galaxies (SMGs; Blain et al. 2002) which are characterized by their detection at $850 \mu\text{m}$ with $S_{850} \gtrsim 5 \text{ mJy}$. While SMGs put powerful constraints on galaxy evolution theories and the environments of extreme star formation (Chapman et al. 2005; Greve et al. 2005; Pope et al. 2006; Tacconi et al. 2006; Tacconi et al. 2008), their selection is susceptible to strong temperature biasing (Eales et al. 2000; Blain et al. 2004). At the mean redshift of radio SMGs, $z \sim 2.2$, observations at $850 \mu\text{m}$ sample the Rayleigh–Jeans tail of blackbody emission where the observed flux density may be approximated by $S_{850} \propto L_{\text{FIR}} T_{\text{dust}}^{-3.5}$. Due to the strong dependence on dust temperature, the $850\text{-}\mu\text{m}$ flux density of warm-dust ULIRGs ($T_{\text{d}} \gtrsim 40 \text{ K}$) might be much lower than cooler dust specimens ($T_{\text{d}} = 20\text{--}40 \text{ K}$) thus causing the warmer-dust galaxies to evade submillimetre detection. This selection bias suggests that a large fraction of the $z \sim 2$ ULIRG population has not been accounted for in current work on high- z star formation.

Chapman et al. (2004) describe the first observational effort to identify warm-dust ULIRGs as a population, via the selection of submillimetre-faint radio galaxies (SFRGs) with starburst-consistent rest-UV spectra. While they were thought to be ULIRGs by their similarities to SMGs (similar radio luminosities, optical spectra, stellar masses), without detection in the far-infrared (FIR), there was no direct evidence that their luminosities were in excess of $10^{12} L_{\odot}$. Ideally, detection at shorter wavelengths in the infrared, at $\lambda \leq 500 \mu\text{m}$, must be used to confirm a ULIRG’s luminosity in the absence of submillimetre detection; Casey et al. (2009a) used $70\text{-}\mu\text{m}$ detection to confirm that a subset of the SFRG population contains a dominating warmer-dust component with $\langle T_{\text{d}} \rangle = 52 \text{ K}$. While a population of warm-dust ULIRGs has been shown to exist, some fundamental questions still remain unanswered: are warm-dust ULIRGs in a post-SMG AGN heated phase? Could they be triggered by different mechanisms than the major mergers said to give rise to cold-dust SMGs?

Investigating the molecular gas content is fundamental to the characterization of star formation properties and gas dynamics of a galaxy population. Molecular line transitions from carbon monoxide (CO) are a direct probe of the vast gas reservoirs that are needed to fuel high star formation rates (Frayser et al. 1999; Greve et al. 2005; Tacconi et al. 2006; Chapman et al. 2008; Tacconi et al. 2008). The gas dynamics which are derived from these observations shed light on galaxies’ evolutionary sequences by measuring how disturbed their gas reservoirs are and how long they can maintain their star formation rates with the observed fuel supply. Recent simulation works hint that a ULIRG phase may be triggered by either major merger interactions (e.g. Narayanan et al. 2009) or from steady bombardment from low-mass fragments (e.g. Davé et al. 2010); linking observations with these different evolutionary scenarios is an essential step in understanding galaxy evolution in the early Universe.

In this paper, we present CO molecular gas observations, taken with the IRAM Plateau de Bure Interferometer (PdBI), of 12 SFRGs (and four additional SFRGs from the literature) to compare the population with SMGs and other high-redshift star-forming galaxies. Section 2 describes the sample selection, molecular gas observations and ancillary data, while Section 3 presents our results, in the form of derived gas and star formation quantities of the SFRG sample. Section 4 discusses the gas properties of the sample, compares the population to other high-redshift galaxies and hypothesizes on the role of SFRGs in a broader galaxy evolution context relative to local ULIRGs and SMGs while Section 5 concludes. Throughout, we use a ΛCDM cosmology with $H_0 = 71 \text{ km s}^{-1} \text{ Mpc}^{-1}$, $\Omega_{\Lambda} = 0.73$ and $\Omega_{\text{m}} = 0.27$ (Hinshaw et al. 2009).

2 OBSERVATIONS AND REDUCTION

Our sample is drawn from a set of μJy radio galaxies in the GOODS-N, Lockman Hole, Elais-N2, SSA13 and the UDS fields using the Chapman et al. (2004) selection of SFRGs. They were detected in ultradeep VLA radio maps (Ivison et al. 2002, 2007; Biggs & Ivison 2006; Fomalont et al. 2006) with $S_{1.4\text{GHz}} \gtrsim 15 \mu\text{Jy}$ at $>3\sigma$ with an approximate upper limit of $S_{1.4\text{GHz}} \lesssim 1 \text{ mJy}$ since strong AGN and radio-bright local galaxies were removed from the sample. The μJy radio galaxy population was identified in an effort to isolate bright star formers at high redshift, so only the sources with non-AGN photometric redshifts of $z \gtrsim 1$ were included (e.g. Chapman et al. 2003). Spectroscopic follow-up studies with Keck LRIS revealed starburst spectral features (Chapman et al. 2004; Reddy et al. 2006), mostly at redshifts $z \gtrsim 1$. The SFRGs with the most reliable spectroscopic redshifts (often due to a strong Ly α emission peak, $\sigma_z \lesssim 0.005$) were chosen for CO observations at the IRAM Plateau de Bure Interferometer.

We note that all the galaxies in our sample satisfy the *BzK* ‘active’ galaxy selection criterion (Daddi et al. 2004), and 10/14 satisfy the Dust Obscured Galaxy (DOG) selection (Dey et al. 2008). All SFRGs have poor rest-UV photometry, so their selection with respect to BX/BM (Steidel et al. 2004) is not constrained.

Fig. 1 shows the distribution in radio luminosity of the CO-observed SFRG sample relative to the distributions of parent

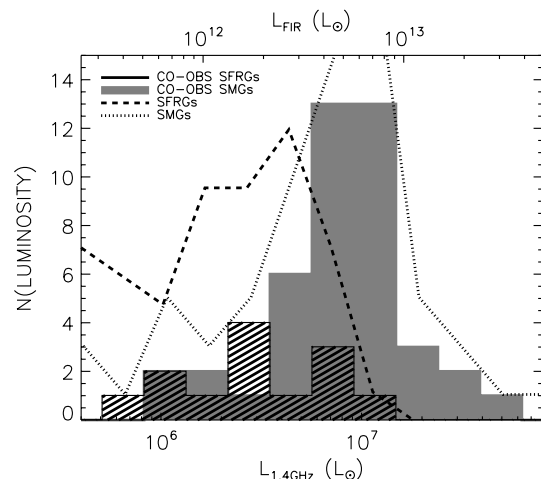


Figure 1. The distribution in radio luminosity (and inferred FIR luminosity) of CO-observed SFRGs (black line-filled) and SMGs (grey filled) relative to the distribution in radio luminosities of their parent populations: spectroscopically confirmed SFRGs (dashed line) and SMGs (dotted line) without CO observations.

SFRGs, CO-observed SMGs and parent SMGs. We note that the CO-observed sample in this paper is about two times less radio luminous than the CO-observed SMGs which were analysed in Neri et al. (2003), Greve et al. (2005) and Tacconi et al. (2006) – an aspect of their selection which traces back to the removal of more luminous spectroscopic AGN from the SFRG sample. The equivalent class of spectroscopic AGN are not removed from the SMG sample since their detection in the FIR provides sufficient evidence that the SMGs are star-formation dominated. This likely represents the most dominant selection bias between the populations; however, we discuss it in more detail in Section 4.6. We also discuss the AGN fraction of SFRGs at length in Section 4.1. While lower luminosity SMGs have been observed with PdBI (representing the low-luminosity tail on the SMGs in Fig 1; Bothwell et al., in preparation), only the published CO-observed SMGs are included in this paper for comparison.

2.1 PdBI observations

Nine SFRGs were observed from 2008 June to 2008 October, while three additional sources were observed in August through October of 2009. The mean redshift of the sample is $z = 1.9 \pm 0.6$.

CO observations were carried out with PdBI in the five dish D-configuration (i.e. compact). We used the 2- and 3-mm receivers tuned to the appropriate frequencies of redshifted CO transitions, as detailed in Table 1. Pointing centres were at the VLA positions of the galaxies, and example phase calibrators which we used were 0221+067, 1044+719, 1418+546, 1308+326 and 0954+658 with flux calibrators like MWC349, 3C84 and 3C345. The synthesized beam size for the configuration varies from ≈ 3 to 6 arcsec FWHM. Receiver noise temperature calibration was obtained every 12 min using the standard hot-/cold-load absorber measurements. The antenna gains were found to be consistent with a standard range of values from 24 to 31 Jy K⁻¹. We estimate the flux density scales to be accurate to about ± 15 per cent.

Data were recorded using both polarizations, offset in frequency, covering a 1.8-GHz bandwidth, except in the cases of RGJ021827, RGJ131207 and RGJ105239 which had 0.9-GHz bandwidth coverage (overlapping polarizations), and RGJ123644 which had 1.6 GHz coverage (semi-overlapping polarizations). RGJ123644 had an uncertain spectroscopic redshift and upon initial observations with a 0.9-GHz bandwidth, a feature was identified at the edge of the bandwidth and subsequent observations were shifted in redshift, thus totalling a 1.6-GHz coverage. The total on-source integration time varied between ~ 4 and 12 h. The data were processed using the GILDAS packages CLIC and MAPPING and analysed with our own IDL-based routines. The rms noise of each object's map is also given in Table 1. For clarity of presentation, we have regridded the data to a spectral resolution of 40 MHz for data with > 1.5 -GHz bandwidth and to 20 MHz for data with < 1.5 -GHz bandwidth. The bandwidths, binsizes and noise properties of the maps are given in Table 1.

The search for CO line detection was performed by integrating all the possible combinations of channels at every location in the observed maps using our own iterative GILDAS script. From the result we measure the data's signal-to-noise ratio (S/N) at all points in the map, and subsequently investigate signal peaks greater than 4σ . If a detection with signal strength $> 4\sigma$ exists within 5 arcsec of the target position, the observed galaxy is classified as detected.

2.1.1 Offset CO detections

Searching for detections within a 5 arcsec radius implies that significant positional offsets are acceptable. In our galaxies, only three of our sources (RGJ021827, RGJ105209 and RGJ105239) have offsets $\gtrsim 2$ arcsec. Nominally, an offset > 2 arcsec would be too large to attribute to the targeted source; however, we note a few factors that can increase the positional uncertainty to ~ 5 arcsec. PdBI D-configuration positional uncertainty is governed by the source S/N [which is proportional to $\text{beamsize}/2(S/N)$, $\lesssim 1$ arcsec, but might diverge at small S/N], the baseline model uncertainty (~ 0.25 arcsec for D-config), and the quality of phase calibration (which can translate to 1.5–3 arcsec seeing). Since the S/N of these galaxies is small, the nominal uncertainty likely increases from ~ 2 to ~ 3 arcsec. It is also possible for the bulk of the gas reservoir in a system to be offset from the primary source of starlight, especially in the case of major mergers. In addition, we have found large positional offsets ~ 5 arcsec with strong $> 5\sigma$ CO detections in the larger samples of SMGs (i.e. CO positional offset from radio centroid; Smail & Bothwell, private communication). Since these detections are centred on the correct redshifts and there does not seem to be other radio/UV/IR sources corresponding with their positions, we treat RGJ021827, RGJ105209 and RGJ105239 as detected; however, we label their spectra and CO maps as 'OFFSET' and list them separately in Table 2, both as tentatively detected and as undetected, giving the upper limits for phase centre observations. We plot them in subsequent figures as detected, although mark them with different symbols to indicate exclusion from key calculations in our analysis.

2.1.2 Remarks on individual sources

RGJ163655, RGJ131236 and ¹²CO($J = 3 \rightarrow 2$) RGJ123711 are taken from Chapman et al. (2008), the pilot study for the sample observed in this paper. These data, when presented in this paper, are different from the spectra and maps presented in Chapman et al. due to a different reduction. We decided to re-reduce their data to be consistent with our reduction, making significant improvements in both phase and amplitude calibration. The differences do not change the results of Chapman et al., but a few changes in minor conclusions are noted later on in the results and discussion. The Chapman et al. CO observations of RGJ131236 were carried out assuming $z = 2.240$; however, more recent rest-UV spectroscopic observations indicate a different rest-UV redshift, $z = 2.224$. The final channel in the data cube might suggest a flux excess at the correct redshift, although we cannot distinguish between a bright line cut-off at the edge, a broad faint line, continuum or noise spike. We treat this source as undetected with the associated noise properties of our observations. We also note that RGJ123711 was observed as a part of Chapman et al. (2008) in ¹²CO($J = 3 \rightarrow 2$), but newer, higher S/N observations in ¹²CO($J = 4 \rightarrow 3$) were taken as a part of this programme. For comparison, we include the Chapman et al. results in Tables 1 and 2. In the re-reduction of RGJ163655 observations, we find a possible companion CO source at the same redshift offset by ~ 8 arcsec to the north-west which is not seen in the Chapman et al. results; however, significant improvements in phase and amplitude calibration have been made since. This source is discussed briefly in Section 3.1. The new data taken for RGJ123711 reveal a marginal ¹²CO($J = 4 \rightarrow 3$) detection for the SMG SMMJ123711.98+621325.7 (also called HDF 255); its integrated CO flux (detected at 4.5σ) is $I_{12\text{CO}(J=4\rightarrow 3)} = 0.54 \pm 0.12$ Jy km s⁻¹; its spectrum and properties will be discussed more

Table 1. PdBI observation properties and FIR, radio data for SFRGs.

Name	z_{opt}	Obs. ^{12}CO Transition	ν_{obs} (GHz)	BW ^a (GHz)	rms _{ct} (mJy)	rms _{ch} (mJy)	Bin (MHz)	Beamsize (arcsec \times arcsec, $^{\circ}$)	i (mag)	S_{24} (mJy)	S_{70} (mJy)	S_{350} (mJy)	S_{850} (mJy)	S_{1200} (mJy)	$S_{1.4\text{ GHz}}$ (μJy)
RGJ021827	1.361	2 \rightarrow 1	97.810	0.9	0.11	0.71	20	7.1 \times 4.4, 150 $^{\circ}$	24.5	–	–	–	<3.5	–	83.7 \pm 7.0
RGJ105209	2.112	3 \rightarrow 2	111.117	1.8	0.08	0.56	40	5.1 \times 3.9, 133 $^{\circ}$	>25.1	167 \pm 47	<1.8	<33	<4.2	<1.8	34.5 \pm 5.5
RGJ105239	1.819	2 \rightarrow 1	81.780	0.9	0.10	0.65	20	6.1 \times 5.1, 98 $^{\circ}$	22.8	150 \pm 30	<6.2	–	<1.8	<1.4	25.6 \pm 6.2
RGJ123642	3.661	4 \rightarrow 3	98.915	1.8	0.08	0.56	40	7.6 \times 3.9, 49 $^{\circ}$	25.9	<15	<1.9	–	<3.4	<0.9	20.1 \pm 8.2
RGJ123644	2.095	3 \rightarrow 2	111.727	1.6	0.10	0.66	40	6.6 \times 3.6, 46 $^{\circ}$	24.2	123 \pm 29	<1.8	–	<3.6	<2.8	39.6 \pm 8.7
RGJ123645	1.433	2 \rightarrow 1	94.755	1.8	0.06	0.39	40	5.0 \times 4.8, 86 $^{\circ}$	23.5	172 \pm 34	4.8 \pm 0.4	–	<10.8	<1.6	83.4 \pm 9.8
RGJ123653	1.275	2 \rightarrow 1	101.335	1.8	0.08	0.56	40	4.9 \times 4.0, 75 $^{\circ}$	22.7	164 \pm 33	6.6 \pm 0.4	–	<1.2	<0.7	86.7 \pm 8.3
RGJ123707	1.489	2 \rightarrow 1	92.623	1.8	0.08	0.56	40	6.1 \times 4.4, 65 $^{\circ}$	22.9	588 \pm 63	<1.7	–	<3.2	<1.7	24.1 \pm 8.6
RGJ123711	1.996	4 \rightarrow 3	153.885	1.8	0.09	0.60	40	4.2 \times 2.7, 53 $^{\circ}$	24.2	473 \pm 57	1.4 \pm 0.4	<24	<2.4	<4.4	126.3 \pm 8.6
RGJ123718	1.512	2 \rightarrow 1	91.775	1.8	0.06	0.39	40	5.5 \times 4.4, 80 $^{\circ}$	23.1	73 \pm 23	<1.7	–	<3.8	<0.6	15.2 \pm 6.8
RGJ131207	1.532	2 \rightarrow 1	91.050	0.9	0.12	0.82	20	5.8 \times 4.3, 127 $^{\circ}$	24.8	105 \pm 15 \ddagger	–	–	<3.8	–	44.9 \pm 2.4
RGJ131208	2.237	3 \rightarrow 2	106.826	1.8	0.07	0.44	40	4.5 \times 4.0, 82 $^{\circ}$	25.2	279 \pm 14 \ddagger	–	<82	<3.0	–	37.6 \pm 4.0
Lit SFRGs:															
RGJ123626 ^a	1.465	2 \rightarrow 1	93.525	1.8	0.09	0.78	12		24.3	94 \pm 26	<1.7	–	<7.0	<1.1	37.9 \pm 9.3
RGJ123710 ^a	1.522	2 \rightarrow 1	91.411	1.8	0.10	0.87	12		24.2	227 \pm 39	3.9 \pm 0.5	–	<1.8	<1.2	38.3 \pm 10.1
(RGJ123711 ^b	1.996	3 \rightarrow 2	115.410	0.9	0.19	1.34	18								
RGJ131236 ^b	2.224	3 \rightarrow 2	106.727	0.9	0.10	0.69	18		24.1	–	–	–	<2.2	–	43.9 \pm 7.1
RGJ163655 ^b	2.186	3 \rightarrow 2	108.536	1.2	0.07	0.49	20		23.5	<150	–	13.7 \pm 6.9	<2.2	–	48.7 \pm 4.3

Note. The top 12 sources were observed in our programme and the bottom five CO-observed SFRGs are taken from the literature: ^afrom Daddi et al. (2008) and ^bfrom Chapman et al. (2008). BW^a denotes the bandwidth of observations. Non-detections are 2σ upper limits, magnitudes are in AB and ellipses denote that no data have been taken of that galaxy at the given wavelength (24, 70, 350 and 1200 μm). RGJ123711 is listed twice, once for its observations taken under our programme, and once for the observations discussed in Chapman et al. (2008). The 24- μm flux densities of the SSA13 field sources are marked by †: they are derived from IRS spectral observations since no MIPS imaging exists for this field (Casey et al., in preparation). The rms_{ct} is the noise of the CO observations averaged over the bandwidth of observations (also over one beamsize at phase centre), while rms_{ch} is the noise per frequency channel which has width with size bin, in MHz. The frequency bins are chosen for optimum presentation of the spectra, as shown in Fig. 3 and are based on bandwidth. The uncertainties on the radio flux densities are errors on flux integrated measurements and not statistical errors. RGJ021827 was targeted at a redshift of 1.357, which is the redshift of a nearby source; the correct UV spectroscopic redshift is 1.361, which is within the bandwidth of our CO observations. RGJ163655 has an H α redshift of 2.192 and a UV redshift of 2.186, both within the bandwidth of the literature observations. The redshift for RGJ131236 has been corrected from an earlier measurement of 2.240. Its CO observations were taken at 2.240, so unfortunately the CO[3–2] line at 2.224 falls at the edge of the PdBI bandwidth, which makes it difficult to put constraining limits on its CO emission.

Table 2. Derived gas properties of submillimetre-faint ULIRGs.

Name	z_{optical}	z_{CO}	Obs. ^{12}CO Transition	S/N	I_{CO} (Jy km s $^{-1}$)	L'_{CO} (K km s $^{-1}$ pc 2)	$I_{\text{CO}(1-0)}$ (Jy km s $^{-1}$)	$L'_{\text{CO}(1-0)}$ (K km s $^{-1}$ pc 2)	ΔV_{CO} (km s $^{-1}$)
CO-detected SFRGs									
RGJ123626.53+620835.3	1.465	1.465 ± 0.002	$^{12}\text{CO}(J = 2 \rightarrow 1)$	6.8	0.60 ± 0.09	$(1.7 \pm 0.3) \times 10^{10}$	0.20 ± 0.10	$(2.3 \pm 0.3) \times 10^{10}$	~350
RGJ123644.13+621450.7	2.095	2.090 ± 0.001	$^{12}\text{CO}(J = 3 \rightarrow 2)$	4.3	0.79 ± 0.22	$(1.9 \pm 0.5) \times 10^{10}$	0.12 ± 0.03	$(2.5 \pm 0.7) \times 10^{10}$	214 ± 132
RGJ123645.88+620754.2	1.433	1.434 ± 0.001	$^{12}\text{CO}(J = 2 \rightarrow 1)$	4.1	0.64 ± 0.17	$(1.8 \pm 0.5) \times 10^{10}$	0.22 ± 0.06	$(2.4 \pm 0.6) \times 10^{10}$	320 ± 144
RGJ123710.60+622234.6	1.522	1.522 ± 0.002	$^{12}\text{CO}(J = 2 \rightarrow 1)$	8.9	0.85 ± 0.10	$(2.5 \pm 0.3) \times 10^{10}$	0.28 ± 0.08	$(3.3 \pm 0.3) \times 10^{10}$	~250
RGJ123711.34+621331.0	1.996	1.988 ± 0.002	$^{12}\text{CO}(J = 4 \rightarrow 3)$	6.5	1.02 ± 0.16	$(1.3 \pm 0.2) \times 10^{10}$	0.10 ± 0.02	$(2.0 \pm 0.4) \times 10^{10}$	558 ± 121
		1.996 ± 0.002	$^{12}\text{CO}(J = 4 \rightarrow 3)$	7.3	0.61 ± 0.08	$(7.8 \pm 1.1) \times 10^9$	0.06 ± 0.01	$(1.2 \pm 0.1) \times 10^{10}$	318 ± 86
		Combined:	$^{12}\text{CO}(J = 4 \rightarrow 3)$	10.4	1.87 ± 0.18	$(2.4 \pm 0.2) \times 10^{10}$	0.19 ± 0.02	$(3.7 \pm 0.4) \times 10^{10}$	(1400 ± 100)
		1.995	$^{12}\text{CO}(J = 3 \rightarrow 2)$	3.2	0.70 ± 0.22	$(1.5 \pm 0.5) \times 10^{10}$	0.10 ± 0.03	$(2.0 \pm 0.6) \times 10^{10}$	–
(RGJ123711.34+621331.0	1.996	2.237 ± 0.001	$^{12}\text{CO}(J = 3 \rightarrow 2)$	5.6	0.88 ± 0.15	$(2.4 \pm 0.5) \times 10^{10}$	0.13 ± 0.02	$(3.3 \pm 0.6) \times 10^{10}$	439 ± 84
RGJ131208.34+424144.4	2.237	2.187 ± 0.002	$^{12}\text{CO}(J = 3 \rightarrow 2)$	4.9	0.29 ± 0.06	$(7.8 \pm 1.6) \times 10^9$	0.04 ± 0.01	$(1.0 \pm 0.2) \times 10^{10}$	252 ± 40
RGJ163655.04+410432.0	2.186	1.820 ± 0.001	$^{12}\text{CO}(J = 3 \rightarrow 2)$	4.2	0.44 ± 0.10	$(1.1 \pm 0.2) \times 10^{10}$	0.15 ± 0.04	$(1.5 \pm 0.3) \times 10^{10}$	557 ± 107
Offset-CO SFRGs									
(as detections)									
RGJ021827.35–050055.9	1.361	1.362 ± 0.002	$^{12}\text{CO}(J = 2 \rightarrow 1)$	4.2	0.44 ± 0.10	$(1.1 \pm 0.2) \times 10^{10}$	0.15 ± 0.04	$(1.5 \pm 0.3) \times 10^{10}$	557 ± 107
RGJ105209.31+572202.8	2.112	2.113 ± 0.001	$^{12}\text{CO}(J = 3 \rightarrow 2)$	4.6	1.12 ± 0.25	$(2.8 \pm 0.6) \times 10^{10}$	0.17 ± 0.04	$(3.7 \pm 0.7) \times 10^{10}$	446 ± 85
RGJ105239.84+572509.1	1.819	1.820 ± 0.001	$^{12}\text{CO}(J = 2 \rightarrow 1)$	4.7	0.57 ± 0.12	$(2.5 \pm 0.5) \times 10^{10}$	0.19 ± 0.04	$(3.3 \pm 0.7) \times 10^{10}$	498 ± 157
(as non-detections)									
RGJ021827.35–050055.9	1.361	–	$^{12}\text{CO}(J = 2 \rightarrow 1)$	–	<0.20	< 4.9×10^9	<0.07	< 6.5×10^9	–
RGJ105209.31+572202.8	2.112	–	$^{12}\text{CO}(J = 3 \rightarrow 2)$	–	<0.21	< 5.1×10^9	<0.03	< 6.9×10^9	–
RGJ105239.84+572509.1	1.819	–	$^{12}\text{CO}(J = 2 \rightarrow 1)$	–	<0.20	< 8.5×10^9	<0.07	< 1.1×10^{10}	–
CO-undetected SFRGs									
RGJ123642.96+620958.1	3.661	–	$^{12}\text{CO}(J = 4 \rightarrow 3)$	–	<0.22	< 7.8×10^9	<0.02	< 1.3×10^{10}	–
RGJ123653.37+621139.6	1.275	–	$^{12}\text{CO}(J = 2 \rightarrow 1)$	–	<0.22	< 4.7×10^9	<0.07	< 6.2×10^9	–
RGJ123707.82+621057.6	1.489	–	$^{12}\text{CO}(J = 2 \rightarrow 1)$	–	<0.23	< 6.7×10^9	<0.08	< 8.9×10^9	–
RGJ123718.58+621315.0	1.512	–	$^{12}\text{CO}(J = 2 \rightarrow 1)$	–	<0.15	< 4.7×10^9	<0.05	< 6.3×10^9	–
RGJ131207.74+423945.0	1.532	–	$^{12}\text{CO}(J = 2 \rightarrow 1)$	–	<0.24	< 7.3×10^9	<0.08	< 9.8×10^9	–
RGJ131236.01+424044.1	2.224	–	$^{12}\text{CO}(J = 3 \rightarrow 2)$	–	<0.18	< 4.7×10^9	<0.03	< 6.3×10^9	–

Note. The observed CO properties of the sample. The top seven sources have clean $>4\sigma$ detections of CO at phase centre, the next three sources (labelled ‘Offset’) have CO detections at the correct redshift but offset ~ 3 –5 arcsec from phase centre, and the remaining six sources are undetected in CO. L'_{CO} and I_{CO} are given for the observed CO transition, which does not depend on source excitation. Then assuming the Weiss et al. (2007) SMG excitation ladder (see text for description), we convert to $I_{\text{CO}(1-0)}$ and $L'_{\text{CO}(1-0)}$, which is given in the subsequent columns. ΔV_{CO} is the FWHM of the fitted feature shown in Fig. 2. The SFRG with a double-peaked feature (RGJ123711) has the details of each feature listed separately. $I_{\text{CO}} 2\sigma$ limits for undetected SFRGs are calculated assuming a $\Delta V_{\text{CO}} = 320$ km s $^{-1}$ (the mean FWHM of the detected-SFRG sample).

at length in a paper summarizing CO properties of observed SMGs to date (Bothwell et al., in preparation).

2.2 Archival observations

This paper also includes the CO-observations of two additional SFRGs from the literature. Daddi et al. (2008) analysed RGJ123710 and RGJ123626 as being high-redshift normal spiral galaxies which have very low star formation efficiencies (a study expanded upon in Daddi et al. 2010). The Daddi et al. survey has shown that the active *BzK* galaxies have a significant overlap with the SFRG population since their CO sources require radio detection, thus they have ULIRG luminosities implied from the radio. Both RGJ123710 and RGJ123626 are selected as SFRGs via the Chapman et al. (2004) method and are likely very luminous star formers, with higher SFRs than most active *BzK*s. RGJ123710 has also been detected at 70 μm (Casey et al. 2009a), directly confirming that it is a ULIRG with a warm dust temperature. Interpreting the *BzK* active galaxy population as ULIRGs rather than ‘high-*z* normal spirals’ is perhaps sensible for these reasons.

2.3 Multiwavelength data

Radio fluxes from VLA B-array maps (5 arcsec resolution) are taken from Richards (2000) and Morrison et al. (2008), where the uncertainty represents the error in the extracted flux measurement rather than statistical error. High-resolution observations from the Multi-Element Radio Linked Interferometer Network (MERLIN; Thomasson 1986) were obtained for the sources in GOODS-N as described in Muxlow et al. (2005), and a combined MERLIN+VLA map was constructed with an rms noise of 4.0 $\mu\text{Jy beam}^{-1}$. A similar map was constructed in Lockman Hole with an rms noise of 4.5 $\mu\text{Jy beam}^{-1}$ (Biggs & Ivison 2008). The combined MERLIN+VLA maps have positional accuracies of tens of mas and restoring circular beam sizes of 0.4 arcsec (GOODS-N) and 0.5 arcsec (Lockman Hole).

RGJ105209, RGJ123711 and RGJ131208 were all observed at 350 μm with the SHARC2 camera (Dowell et al. 2003) on the Caltech Submillimeter Observatory and reduced with CRUSH software (Kovács et al. 2006). With on-source integration times of 950, 1080 and 200 s, RGJ105209, RGJ123711 and RGJ131208 showed flux densities of 19 ± 7 mJy, 6 ± 9 mJy and 48 ± 17 mJy, respectively. A fourth SFRG, RGJ163655, was observed at 350 μm with the CSO previously (Chapman et al. 2008). None is detected at $>3\sigma$. While making ground-based 350- μm observations is laborious and dependent on the weather conditions being the best of them ($\tau_{\text{CSO}} < 0.06$, measured at 225 GHz), the relative depth of our observations is comparable to the expected confusion limits for the *Herschel Space Observatory* at 350 μm . While *Herschel* will detect >40 mJy 350- μm sources at high-*z* regularly, sources with flux density $\lesssim 20$ mJy will need follow-up from ground-based facilities like the CSO for more precise flux density estimates and will also need better SED constraints.

The 1200 μm flux limits for GOODS-N and Lockman Hole come from the Max-Planck Millimeter Bolometer (MAMBO, with a mean rms of ~ 0.8 mJy; Greve et al. 2008) and 850 μm flux limits from the Submm Common User Bolometric Array (SCUBA, with a mean rms of ~ 1.6 mJy; Borys et al. 2003; Coppin et al. 2006). All fields are covered by *Spitzer* IRAC (3.6, 4.5, 5.8 and 8.0 μm) and MIPS (24 and 70 μm), however at greatest depths in all bands in GOODS-N. Optical photometry in GOODS-N is from

the *HST* ACS¹ using the F435W, F606W, F814W and F850LP filters (*B*, *V*, *i* and *z* bands). The Lockman Hole has *HST* ACS F814W (PI: Chapman *HST* 7057) in addition to extensive optical photometry from Subaru/Suprime-Cam (Miyazaki et al. 2002). X-ray fluxes are measured from the *Chandra/XMM* maps of GOODS-N (Alexander et al. 2003), Lockman Hole (Brunner et al. 2008), SSA13 (Mushotzky et al. 2000) and SXDF (Ueda et al. 2008).

2.4 RGJ105209

Recent work on the mid-infrared spectra of SFRGs from the *Spitzer* InfraRed Spectrograph (IRS) (Casey et al., in preparation) has revealed that the 24- μm source that lies at the position of RGJ105209 (at the radio position) has a dominant PAH redshift of 2.37, in contrast to the CO and UV spectroscopic redshift of 2.112. We suspect that two different systems overlap each other to create these discrepant redshifts, but note that only one source is visible in the rest-UV. The high-resolution MERLIN+VLA radio imaging also shows only one point source slightly offset, 1.2 arcsec, from the UV source. Due to positional uncertainties, it is difficult to pinpoint which source is generating the radio emission. For that reason, we assume in this paper that the radio is associated with the 2.112 CO source. We note that similar positional overlap phenomena have occurred with star-forming galaxies before, for example there are several examples of sources with two distinct redshifts for one continuum source in the surveys of Steidel et al. (2004) and Reddy et al. (2006, 2008), and the density of bright star forming $z \sim 2$ sources is high enough that overlap will occur with non-negligible probability.

3 ANALYSIS AND RESULTS

3.1 Derived properties from CO data

Table 2 lists the integrated line fluxes and limits for all the SFRGs in our sample. Out of the 12 sources in our observing program, seven SFRGs were detected at $\gtrsim 4\sigma$. Including the literature SFRGs, 10/16 are CO-detected, and one ‘undetected source’ has insufficient data to determine detection (RGJ131236, with an ambiguous redshift). Three of our detected sources have significant positional offsets from their radio positions, thus we have classified these as ‘tentative’ detections in Table 2 and excluded them from calculations in our analysis. The detection fraction of SFRGs, 10/16 (63 per cent, including offset sources), is similar to the detection fraction of SMGs in Greve et al. (2005) and Coppin et al. (2008).

While we do not expect continuum flux from any SFRG, we test whether it is based on FIR detection limits. To test the detectability of blackbody continuum radiation, we interpolate the best-fitting FIR SEDs (see Section 3.6) to estimate the flux density at the frequency of PdBI observations ($\nu_{\text{obs}} = 80\text{--}150$ GHz). All the SFRGs in the sample have estimated continuum flux densities < 0.13 mJy, which is of the order of the rms noise in our CO spectra, thus not detectable.

Each remaining SFRG spectrum was fit with a three-parameter Gaussian using a least-squares fitting algorithm, where the

¹ Based on observations made with the NASA/ESA *Hubble Space Telescope*, and obtained from the Hubble Legacy Archive, which is a collaboration between the Space Telescope Science Institute (STScI/NASA), the Space Telescope European Coordinating Facility (STECF/ESA) and the Canadian Astronomy Data Centre (CADAC/NRC/CSA).

spectral noise is simulated as a function of the rms channel noise (see Coppin et al. 2007, for details). Since no detectable continuum emission is expected we do not fit line profiles with constant baselines. Fig. 2 shows the velocity-averaged spatial maps of the millimetre-line observations (with VLA centroids marked with crosses) and Fig. 3 shows the extracted spectra of the CO detections with overlaid Gaussian fits and the original optical spectroscopic redshifts. The 2D maps for the CO-detected SFRGs are integrated over the channel range which produces the highest signal-to-noise ratio line profile in the spectrum. The 2D maps of the undetected sample are integrated over all velocity channels. The CO-detected SFRGs have CO redshifts, which agree with their optical spectroscopic features. Every spectrum was also tested against two three-parameter Gaussian fits (i.e. a double-peaked line) in a χ -squared goodness-of-fit algorithm. Only one galaxy's line fits were significantly improved by fitting to a double-peaked Gaussian. The detection of RGJ123711 is double-peaked with one component centred at $z_{\text{CO}} = 1.988$ and the other at $z_{\text{CO}} = 1.996$, which bracket its optical redshift ($z = 1.995$). The line properties of both components of RGJ123711 are listed separately in Table 2; the total system is represented by the sum of the two separate gas masses and the sum of dynamical masses (we treat them as separate systems since the peaks are asymmetrical and more likely indicative of a merger than rotating disc). The ratio for double-peaked CO in SFRGs is thus $1/8 \approx 13$ per cent, comparable to $5/30 \approx 17$ per cent for SMGs. The weighted mean linewidth of this sample, excluding 'offset' detections is $320 \pm 80 \text{ km s}^{-1}$ (note that it increases to $370 \pm 110 \text{ km s}^{-1}$ if the offset sources are detections).

The 2σ line intensity limits for the CO-undetected SFRGs are calculated using the following:

$$I_{\text{CO}} < 2 \text{ rms}_{\text{ch}} (\Delta V_{\text{CO}} dv)^{1/2}, \quad (1)$$

where rms_{ch} is the channel noise from Table 1; dv is the spectral resolution, the binsize value given in Table 1 converted to km s^{-1} (as in Boselli, Lequeux & Gavazzi 2002). These limits are given in Table 2. The spatial maps for the undetected SFRGs (in Fig. 2) are integrated over the entire bandwidth of observations. None of the maps is corrected for primary beam attenuation; given the $40 \times 40 \text{ arcsec}^2$ size, the PBA correction is < 2 even for all peripheral areas of the map.

The spatial map for RGJ163655 shows another bright companion CO emitter $\sim 8 \text{ arcsec}$ to the north-west of RGJ163655 not previously identified in the reduction of Chapman et al. (2008). Extraction of its spectrum reveals a line centred on the same frequency as the RGJ163655 $^{12}\text{CO}(J = 3 \rightarrow 2)$ line; however, there are no radio sources or spectroscopically identified sources nearby. If follow-up CO observations of RGJ163655 reveal the same feature in different CO transitions, then high-resolution CO will be needed to precisely measure the companion galaxy's position, and thus its multiwavelength properties.

A lack of multiple CO transition data means many past studies have relied on the assumption of constant brightness temperature to convert between higher transition line luminosities and $L'_{\text{CO}(1-0)}$. However, recent observations of multiple CO transitions in high-redshift galaxies have shown that the transitions are often not in thermal equilibrium (Dannerbauer et al. 2009). The three $z \sim 2.5$ SMGs of Weiss et al. (2007) are consistent with being in thermal equilibrium up to a $J = 3$ transition yet not towards higher- J values, while there are several other high-redshift sources that are much more excited, for example FSC 10214+4724 (Scoville et al. 1995) and APM 08279+5255 (Weiß et al. 2007) which have nearly constant brightness temperatures out to $J = 6$ or much less excited

[ERO J16450+4626 turns over at CO(3-2)]. In this paper we adopt the brightness temperature conversions inferred from the spectral line energy distributions for three SMGs observed in Weiss et al. (2007); explicitly, we assume the following line flux ratios derived from LVG models: $S_{\text{CO}21}/S_{\text{CO}10} = 3.0 \pm 0.1$, $S_{\text{CO}32}/S_{\text{CO}10} = 6.8 \pm 0.5$ and $S_{\text{CO}43}/S_{\text{CO}10} = 10.0 \pm 0.8$. One SFRG has multiple line data (RGJ123711) and can be analysed for its excitation. This work is presented in Section 3.2.

More recent work (Danielson et al. 2010; Ivison et al. 2011) on $^{12}\text{CO}(J = 1 \rightarrow 0)$ observations in SMGs show that the assumption of a constant brightness temperature can lead to underestimations of gas mass by factors of $\sim 2 \times$. They find that the ratio of luminosities between $^{12}\text{CO}(J = 3 \rightarrow 2)$ and $^{12}\text{CO}(J = 1 \rightarrow 0)$ is $r_{3-2/1-0} = 0.55$ and ~ 0.67 , respectively. Our excitation assumption implies a ratio $r_{3-2/1-0} \sim 0.78$, slightly higher than these recent studies, but well within the uncertainties of the $S_{12\text{CO}(J=3-2)}$ measurements of Ivison et al. and Danielson et al. The derived line luminosities for our observations are listed in Table 2, in their observed transition as well as in our conversion to $L'_{\text{CO}(1-0)}$.

3.2 CO excitation of RGJ123711

The observations of RGJ123711 in $^{12}\text{CO}(J = 3 \rightarrow 2)$ and $^{12}\text{CO}(J = 4 \rightarrow 3)$ allow an analysis of the CO excitation in the system. Fig. 4 shows the spectrum of both lines and the proposed CO spectral line energy distribution (SLED) for the source; since the $^{12}\text{CO}(J = 3 \rightarrow 2)$ observations do not cover the entire velocity range of the emitting gas, a direct comparison of the line strengths can only be done in the channels where data overlap (between -700 and 300 km s^{-1}) marked by vertical dashed lines in Fig. 4. The ratio of fluxes is then $S_{\text{CO}[4-3]}/S_{\text{CO}[3-2]} = 1.6 \pm 0.4$. We use Monte Carlo testing to estimate the added uncertainty introduced by not including the missing portion of $^{12}\text{CO}(J = 3 \rightarrow 2)$ (from -1150 to -700 km s^{-1}) and we remeasure this ratio to be $S_{\text{CO}[4-3]}/S_{\text{CO}[3-2]} = 2.0 \pm 0.8$. This agrees with the mean $[4-3]/[3-2]$ ratio observed for SMGs, 1.4 ± 0.2 (Weiss et al. 2007) and the expected ratio, if constant brightness temperature is assumed, is 1.8; however, it appears to be inconsistent with the ratio for the Milky Way, ~ 0.7 (Fixsen et al. 1999).

We contrast this result with those of Weiss et al. (2007), Dannerbauer et al. (2009) and Danielson et al. (2010) in the right-hand panel of Fig. 4. Although we have taken measurements for $J = 3$ and 4 only and the other work is restricted to $J \leq 3$ transitions, we see that RGJ123626 and RGJ123711, the two SFRGs included here, seem to exhibit different excitation levels where RGJ123626 is more consistent with a Milky Way type excitation and RGJ123711 is consistent with the Weiss et al. (2007) SMGs. The issue of gas excitation is essential to the physical interpretation of high- z star formers, and more/multiple line transitions are necessary for a full analysis of the population [e.g. see recent work on low CO transitions, like $^{12}\text{CO}(J = 1 \rightarrow 0)$ in Hainline et al. 2006; Riechers et al. 2006; Carilli et al. 2010; Ivison et al. 2011].

3.3 Gas mass and dynamical mass

To derive H_2 masses we assume the ULIRG H_2/CO gas conversion factor $X = M_{\text{H}_2}/L'_{\text{CO}} = 0.8 M_{\odot} (\text{K km s}^{-1} \text{ pc}^2)^{-1}$ from Downes & Solomon (1998). It is worth noting, however, that the CO to H_2 conversion factor varies substantially depending on the type of source being sampled, and it can range from 0.8 in ULIRGs to 4-5 in normal spiral, late-type galaxies (see discussion in the appendix of Tacconi et al. 2008). The basis of our choice of $X = 0.8 M_{\odot} (\text{K km s}^{-1} \text{ pc}^2)^{-1}$ is based on the merger, or disturbed

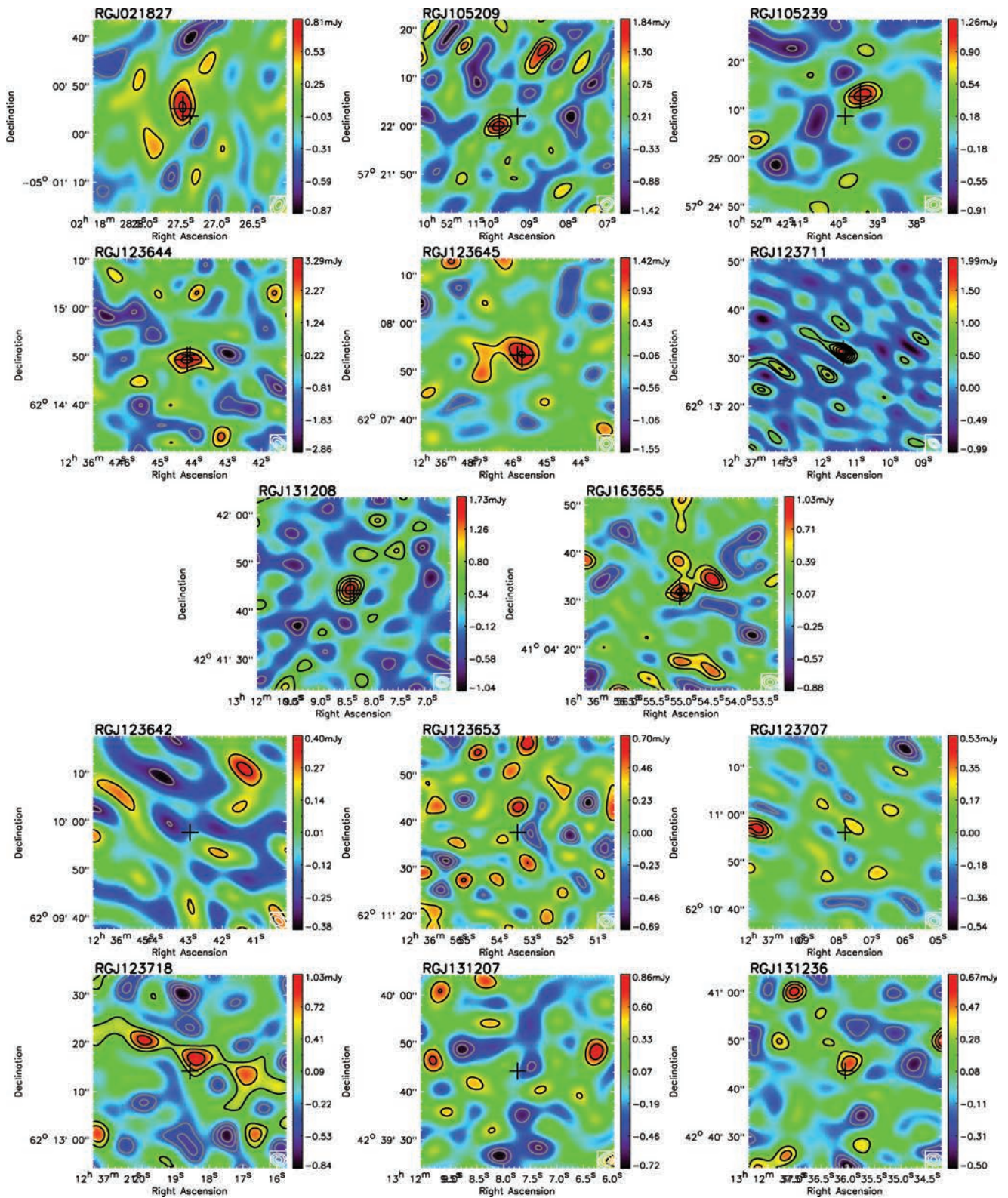


Figure 2. CO maps of SFRG sample in 40×40 arcsec² cutouts, sorted first by detected CO (the first eight are detected), then by RA. For those galaxies detected in CO, the maps are integrated over the optimal velocity channels corresponding to the detected CO line. Black contours are integer multiples of the rms starting at 2σ and thin grey contours are negative integer multiples of rms starting at -2σ . The relative flux scales on the maps are indicated by the colour bars to the right. The spectra in Fig. 3 are extracted within one beamsize (white contours in the lower right, outer contour is FWHM) centred on the highest S/N point in the map (large cross). The three sources at top are labelled ‘Offset’ since their CO peak is ~ 3 – 5 arcsec offset from phase centre, a greater offset than would be caused by positional inaccuracies in the instrument. For galaxies not detected in CO, the maps are integrated over all velocity channels and spectra are extracted from the map centre (small cross).

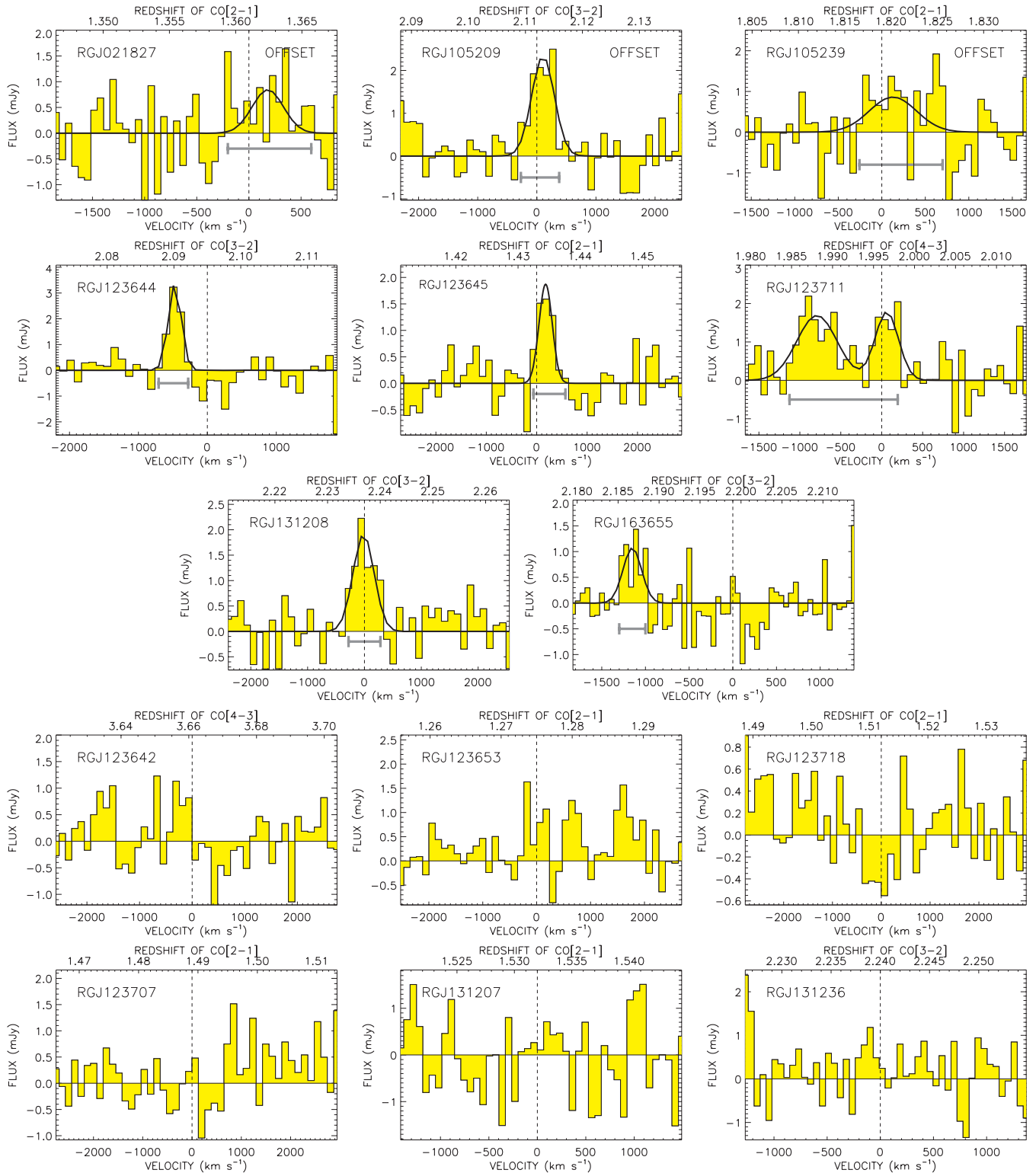


Figure 3. The CO spectra for SFRGs. Spectra are extracted within one beamsize centred on the highest S/N peak for detected sources and on phase centre for non-detections (i.e. the galaxies’ radio positions). Vertical dashed lines indicate the galaxies’ optically derived redshifts. Gray brackets highlight the channel range integrated over to produce the maps in Fig 2. The first three sources labelled ‘Offset’ are detected at large offset positions $\sim 3\text{--}5$ arcsec from phase centre. At bottom right, we show the spectrum for RGJ131236, the SFRG observed in Chapman et al. (2008) at the redshift 2.240; its revised redshift, 2.224, is on the edge of the observed bandwidth.

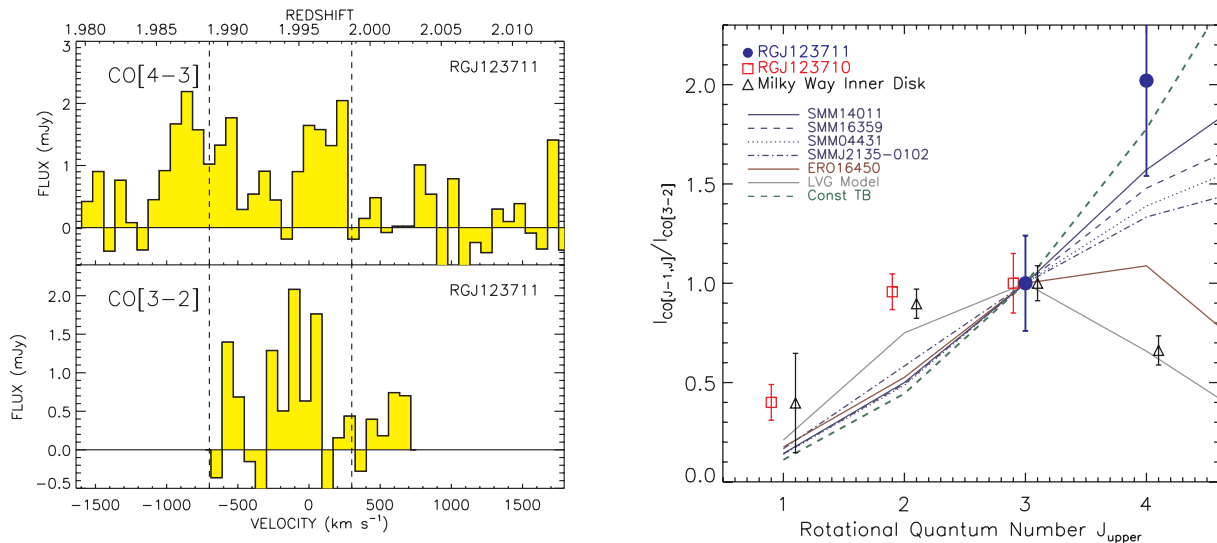


Figure 4. Left: both $^{12}\text{CO}(J = 3 \rightarrow 2)$ and $^{12}\text{CO}(J = 4 \rightarrow 3)$ observed transitions for RGJ123711. Determined from the spectral lines seen in the higher S/N CO[4–3] observation, the velocity range of the emitting region which overlaps in each data set is marked by two vertical dashed lines at -700 km s^{-1} and 300 km s^{-1} . Right: the CO SLED normalized to $I_{\text{CO}[3-2]}$ for RGJ123711 overlaid with literature results from other high-redshift sources (Weiss et al. 2007; Danielson et al. 2010) and the Milky Way (Fixsen, Bennett & Mather 1999). One of these sources is RGJ123710, an SFRG observed by Dannerbauer et al. (2009). We also include LVG model no. 1 from Dannerbauer et al., representing a low-excitation Milky Way type source. By normalizing to $I_{\text{CO}[3-2]}$, we illustrate that it is difficult to draw conclusions on the nature of the CO SLED without observing at least three CO transitions, particularly in the region where the SLEDs are suspected of turning over near CO[4–3].

nature, of ULIRGs and their high star formation rates. Mergers are confined by ram pressure which pervades the whole system, while quiescent discs are confined gravitationally leading to gas fragmenting into clouds (per the jeans mass) and thus much higher ratios of H_2 mass to unit CO. We note that higher gas conversion factors are possible and perhaps likely if SFRGs were to represent an intermediate stage or ‘less extreme’ population of galaxies than SMGs. For this reason, we advise that our H_2 -dependent quantities (M_{H_2} , gas fraction, etc) be taken with a bit of caution, since the full range of galaxy properties and conversion factors (from $X_{\text{CO}} = 0.8$ to 4.5) suggests variations in M_{H_2} of the order of 0.75 dex and variations in gas fractions of the order of 0.6. We also include gas mass estimates for $X_{\text{CO}} = 4.5 M_{\odot} (\text{K km s}^{-1} \text{ pc}^2)^{-1}$ for contrast in Table 3 but proceed with $X_{\text{CO}} = 0.8$ for our analysis. Using $X_{\text{CO}} = 0.8$ for ULIRGs, the mean gas mass of the sample is $(2.1 \pm 0.7) \times 10^{10} M_{\odot}$, which is roughly half the mean H_2 mass of CO-observed SMGs ($5.1 \times 10^{10} M_{\odot}$; Neri et al. 2003; Greve et al. 2005).

Dynamical mass is dependent on the galaxy’s inclination angle; we use the average inclination correction of $\langle \sin i \rangle = 1/2$ (in other words $i = 30^\circ$, corresponding to a random distribution in galaxy angles between 0° and 90°). Thus

$$M_{\text{dyn}} \sin^2 i = \frac{C \sigma^2 r}{G} = 4.215 \times 10^4 C \Delta V_{\text{CO}}^2 r, \quad (2)$$

where $C = 4$ (the value adopted for mergers; Genzel et al. 2003) and r is given in kpc and ΔV_{CO} in km s^{-1} . We note however that the difference between assuming a merger ($C = 4$), spheroid ($C = 5$) or rotating disc ($C = 3.4$) is of the order of the uncertainty in $M_{\text{dyn}} \sin^2 i$ caused by uncertainty in linewidth.

Deriving a dynamical mass is dependent on a resolved spatial size measurement (r in equation 2), which is unfortunately unavailable with this low resolution, 3–6 arcsec beam size (D-configuration PdBI) data. In place of measuring CO sizes explicitly, we assume that the SFRGs of this sample have gas-emitting regions roughly the size of SMGs (Tacconi et al. 2008) which have $R_{1/2} =$

$2 \pm 1 \text{ kpc}$. This is supported by our analysis of high-resolution MERLIN+VLA radio imaging discussed in the next section (in Section 3.4), where SFRGs and SMGs are shown to have similar radio sizes and SFRG sizes average $2.3 \pm 0.8 \text{ kpc}$. Bothwell et al. (2010) have made high-resolution CO observations of RGJ123711 and found its size to be consistent with this assumption (its CO emission extends over 12.6 kpc in one direction and $\sim 5 \text{ kpc}$ in the other, corresponding to a 3.9 kpc effective radius, only 0.2 kpc larger than our measured MERLIN+VLA radio size). RGJ123711 is perceived to be a merging system that has two components of roughly equal spatial extent $\lesssim 2 \text{ kpc}$, thus its effective size is about $\sim 2\times$ larger than the rest of the galaxies in our sample, although we still use the MERLIN+VLA sizes as priors for CO size due to a lack of resolved CO data. For the sources with measured MERLIN+VLA sizes, we use the R_{eff} as the radius r in equation (2), and for sources without MERLIN+VLA data, we assume that r is equal to the mean of the measured MERLIN+VLA sizes, $r = 2.3 \pm 0.8 \text{ kpc}$.

It is important to note that the extent and morphology of the MERLIN+VLA radio emission can affect the interpretation of the dynamical mass estimate. Three objects have large radio/UV offsets or very extended radio emission: RGJ105209 (whose offset is discussed in Section 2.4), RGJ123707 (extended across a $\sim 7 \times 17 \text{ kpc}^2$ area) and RGJ123710 (two knots separated by $\sim 8 \text{ kpc}$). If the CO gas were to trace the MERLIN+VLA morphology perfectly, as is our a priori assumption, then the radius of each knot of radio emission would be used to estimate dynamical masses and they would be summed. Depending on the distribution of these knots, the true dynamical mass would be calculated by considering the size of each knot and the distance separating them; however, within the uncertainty of our measurements and assumptions (e.g. inclination angle, linewidth uncertainty and uncertainty on the value of C) we consider our approach of circularizing the MERLIN+VLA sizes and inferring a radius as accurate. We caution that dynamical masses are potentially slightly underestimated, due to the size and distribution of the CO gas relative to radio emission. For example,

Table 3. Other derived properties of CO-observed SFRGs.

Name	z	L_{FIR} ($10^{12} L_{\odot}$)	SFR _{radio} ($M_{\odot} \text{ yr}^{-1}$)	SFR _{UV} ($M_{\odot} \text{ yr}^{-1}$)	M_{H_2} [U] (M_{\odot})	M_{H_2} [Sp] (M_{\odot})	$M_{\text{dyn}} \sin^2 i$ (M_{\odot})	SFE (L_{\odot}/M_{\odot})	R_{eff} (kpc)	Σ_{SFR} ($\dot{\text{t}}$)	M_{\star} (M_{\odot})	Class ^X	Class ^{IR}	Class ^{CO}
RGJ021827...	1.362	$3.3^{+0.8}_{-0.8}$	570^{+170}_{-120}	9^{+5}_{-3}	1.2×10^{10}	6.5×10^{10}	1.2×10^{11}	280	–	–	2.3×10^{11}	SB	SB	SB
RGJ105209...	2.113	$4.4^{+2.2}_{-1.5}$	750^{+380}_{-250}	20^{+30}_{-10}	3.0×10^{10}	1.7×10^{11}	7.4×10^{10}	150	2.2	49	1.0×10^{11}	SB	SB	SB
RGJ105239...	1.820	$2.2^{+1.8}_{-1.0}$	380^{+300}_{-170}	90^{+30}_{-20}	2.6×10^{10}	1.5×10^{11}	9.6×10^{10}	80	2.3	23	1.2×10^{11}	SB	SB	SB
RGJ123626...	1.465	$1.9^{+1.5}_{-0.5}$	320^{+250}_{-140}	7^{+5}_{-3}	1.8×10^{10}	1.0×10^{11}	5.8×10^{10}	110	2.8	13	2.8×10^{10}	SB	SB	SB
RGJ123642...	3.661	$1.1^{+1.7}_{-0.7}$	1900^{+3000}_{-1100}	30^{+20}_{-10}	$<1.0 \times 10^{10}$	$<5.9 \times 10^{10}$	–	>110	1.4	310	4.1×10^{10}	SB+	SB	SB
RGJ123644...	2.090	$5.0^{+3.5}_{-2.1}$	850^{+600}_{-350}	30^{+30}_{-20}	2.0×10^{10}	1.1×10^{11}	2.1×10^{10}	250	2.7	37	1.1×10^{11}	SB+	SB+	SB
RGJ123645...	1.434	$3.8^{+1.4}_{-1.0}$	660^{+250}_{-180}	30^{+8}_{-6}	1.9×10^{10}	1.1×10^{11}	5.2×10^{10}	200	3.0	23	4.9×10^{10}	SB	SB	SB
RGJ123653...	1.275	$2.9^{+0.9}_{-0.7}$	500^{+160}_{-120}	40^{+10}_{-10}	$<5.0 \times 10^9$	$<2.8 \times 10^{10}$	–	>580	2.8	20	3.6×10^{10}	SB	AGN	SB+
RGJ123707...	1.489	$1.2^{+1.6}_{-0.7}$	210^{+280}_{-120}	50^{+20}_{-10}	$<7.1 \times 10^9$	$<4.0 \times 10^{10}$	–	>170	1.3	39	2.3×10^{10}	SB+	SB	SB
RGJ123710...	1.522	$2.1^{+1.8}_{-1.0}$	350^{+310}_{-170}	10^{+5}_{-5}	2.7×10^{10}	1.5×10^{11}	2.0×10^{10}	80	1.9	30	2.4×10^{10}	SB	SB	SB
RGJ123711...	1.996	$8.8^{+6.1}_{-3.6}$	1500^{+1000}_{-600}	30^{+10}_{-9}	3.0×10^{10}	1.7×10^{11}	1.1×10^{11}	290	3.7	34	1.2×10^{11}	SB+	AGN	SB
RGJ123718...	1.512	$0.8^{+1.5}_{-0.5}$	140^{+250}_{-90}	40^{+10}_{-10}	$<5.0 \times 10^9$	$<2.8 \times 10^{10}$	–	>160	1.1	36	1.6×10^{11}	SB	AGN	SB
RGJ131207...	1.532	$2.5^{+0.6}_{-0.5}$	420^{+100}_{-80}	9^{+7}_{-4}	$<7.8 \times 10^9$	$<4.4 \times 10^{10}$	–	>320	–	–	6.0×10^9	SB	SB	SB
RGJ131208...	2.237	$5.6^{+1.9}_{-1.4}$	960^{+330}_{-250}	20^{+9}_{-6}	2.6×10^{10}	1.5×10^{10}	7.5×10^{10}	220	–	–	1.8×10^{10}	SB	AGN	SB
RGJ131236...	2.224	$6.6^{+3.3}_{-2.2}$	1100^{+600}_{-400}	40^{+20}_{-20}	$<5.0 \times 10^9$	$<2.8 \times 10^{10}$	–	>1300	–	–	2.4×10^{10}	AGN	SB	AGN
RGJ163655...	2.187	$6.8^{+2.1}_{-1.6}$	1200^{+400}_{-300}	70^{+40}_{-30}	8.0×10^9	4.5×10^{10}	2.5×10^{10}	850	–	–	4.1×10^{10}	SB	SB+	AGN

Note. Derived gas properties of SFRGs. L_{FIR} is derived from radio luminosity, and the associated SFR is thus labelled SFR_{radio}. Conversion to gas mass assumes the typical ULIRG conversion factor $X = 0.8 M_{\odot} (\text{K km s}^{-1} \text{ pc}^2)^{-1}$ (Downes & Solomon 1998) for M_{H_2} [U], the default assumption of gas mass for this sample, although we note that higher conversion factors [$\sim 4.5 M_{\odot} (\text{K km s}^{-1} \text{ pc}^2)^{-1}$] might be appropriate for a subset of these galaxies which exhibit normal spiral galaxy characteristics (see Daddi et al. 2010), and these gas masses are given in M_{H_2} [Sp]. The total dynamical mass is calculated by assuming a size of CO emission, which we do not directly measure, but assume is equal to the effective radius of radio emission, given as R_{eff} , and when radio is not available we assume a radius of ~ 2.3 kpc, the mean MERLIN+VLA radius, consistent with SMG sizes. The star formation efficiency (SFE) is SFR_{radio} divided by the ULIRG molecular gas mass, M_{H_2} . SFR_{UV} has not been corrected for extinction. The star formation rate density, Σ_{SFR} , has units of $M_{\odot} \text{ yr}^{-1} \text{ kpc}^{-2}$ ($\dot{\text{t}}$). Since these galaxies were selected in the radio, we provide a measure of their starburst and AGN content by classifying them into starburst (SB), AGN and starburst/AGN mix (SB+) in five separate AGN selection criteria. Class^X marks any galaxy with X-Ray luminosity $> 5 \times 10^{43} \text{ erg s}^{-2}$ as ‘AGN’, $< 1 \times 10^{43} \text{ erg s}^{-2}$ as ‘SB’, and intermediate luminosity galaxies as ‘SB+’. X-ray data are taken from Alexander et al. (2003), Brunner et al. (2008), Ueda et al. (2008) and Mushotzky et al. (2000). Class^{IR} marks galaxies with significant 8- μm flux excess (relative to the stellar population fit) as ‘AGN’, galaxies with marginally significant $< 2\sigma$ 8- μm excess as ‘SB+’ and galaxies with no 8- μm excess as ‘SB’ (see Fig. 6). Class^{CO} marks galaxies with unusually high FIR-to-CO ratios as ‘AGN’ [$\log(L_{\text{FIR}}/L'_{\text{CO}}) > 2.7$], ‘SB+’ [$2.5 < \log(L_{\text{FIR}}/L'_{\text{CO}}) < 2.7$], and at low FIR-to-CO ratios, ‘SB’ [$\log(L_{\text{FIR}}/L'_{\text{CO}}) > 2.5$]. A fourth class may be defined as a measure of the star formation rate density, Σ_{SFR} ; all of the galaxies for which we have Σ_{SFR} measurements satisfy the ‘SB’ criteria, however, with star formation densities $< 200 M_{\odot} \text{ yr}^{-2}$. A fifth class is defined by their rest-UV/optical spectroscopic properties, which, by the method of their selection, is uniformly ‘SB’.

radio sizes are potentially inconsistent with CO sizes, as with the B-configuration data of RGJ123626 and RGJ123710 presented in Daddi et al. (2010), which suggest larger dynamical mass estimates by a factor proportional to the radius.

When applied to the whole SFRG sample, we derive a median SFRG dynamical mass of $M_{\text{dyn}} = (7.2^{+6.7}_{-3.4}) \times 10^{10} M_{\odot} / (\sin^2 i) \approx 2.9 \times 10^{11} M_{\odot}$. The same value of C is used to compare with the mean dynamical mass of SMGs, which is $M_{\text{dyn}}(\text{SMG}) = (1.5^{+1.4}_{-0.4}) \times 10^{11} M_{\odot} / (\sin^2 i) \approx 6.0 \times 10^{11} M_{\odot}$.

3.4 MERLIN+VLA radio morphology

We use the high-resolution MERLIN+VLA radio maps to map the extension of starburst emission and assess the contribution of AGN by considering their radio morphology, which is shown as contour overlays on optical imaging in Fig. 5. With resolutions of 0.4 and 0.5 arcsec per beam (for GOODS-N and the Lockman Hole, respectively), the smallest resolvable structure at $z \sim 1.5$ would be 4–5 kpc across. The typical size of an AGN emission region in a μJy radio galaxy at $z > 1$ (see Casey et al. 2009b) at radio wavelengths is much less than 1 kpc, implying that an AGN-dominated source would be completely unresolved in MERLIN+VLA radio maps (e.g. as seen in the high stellar mass, giant elliptical systems of Casey et al. 2009b). Fig. 5 shows that each of these galaxies has extended emission regions on large scales irregularly spread across large regions of the galaxy, suggestive of spatially distributed star formation, unlikely to be generated by AGN. About 10–60 per cent of the total flux from the source is estimated to be resolved out by the high-resolution imaging, which is dependent on the galaxies' extended or compact morphologies. We measure an effective radius of the star-forming area by isolating the regions where MERLIN+VLA radio emission is significant to $>3\sigma$, and we then take the square root of the surface area over π (effectively circularized), R_{eff} , which is given in Table 3. While the morphologies are irregular (and are not in fact circular), we find that the effective radii average 2.3 ± 0.8 kpc, which agrees with the size measurements of SMGs in Biggs & Ivison (2008) and Chapman et al. (2004). We use the agreement of MERLIN+VLA SFRG and SMG sizes to partly justify our assumption of similar CO sizes between the populations.

Since as much as 60 per cent of the radio flux can be resolved out in the high-resolution maps, we caution that this effective radius might be an underestimate, and that it could increase by factors of 1.1–1.5 \times if all of the flux is accounted for; however, this adjustment is not made to our effective radii measurements since it is highly uncertain and relies on assumptions of the distribution of star formation activity on the outskirts of each source. Similarly, this underestimation of effective radius would propagate to the derivation of dynamical masses.

3.5 Star formation rates, densities and efficiencies

We estimate SFRs from VLA radio luminosities, using the radio/FIR correlation for star-forming galaxies (e.g. Helou, Soifer & Rowan-Robinson 1985; Condon 1992; Sanders & Mirabel 1996):

$$L_{\text{FIR}} = (3.583 \times 10^{-48}) D_L^2 S_{1.4} (1+z)^{(1-\alpha)}, \quad (3)$$

where D_L is luminosity distance in cm, L_{FIR} is evaluated from 8 to 1000 μm and is in L_{\odot} , $S_{1.4}$ is the radio flux density at 1.4 GHz in units of μJy . A Salpeter initial mass function is assumed. The factor of $(1+z)^{(1-\alpha)}$ accounts for bandwidth compression and the radio K -correction to the rest-frame luminosity; α is the synchrotron slope index, here taken to be 0.75 (Yun, Reddy & Condon 2001). Since

this is an empirical relation defined by the mean ratio q between FIR and radio luminosities, there are a few different versions in use in the literature. This relation uses the bolometric ratio between FIR flux and radio flux of $q_{\text{IR}} = 2.46$ (e.g. Casey et al. 2011; Ivison et al. 2010a,b). The relation is traditionally defined by $q = 2.35$ (Sanders & Mirabel 1996) and was used by Chapman et al. (2005) to calculate FIR luminosities for the redshift-identified SMGs (only differing by factors of 20 per cent between different assumed q ratios). In most cases, the FIR luminosities derived from the radio are consistent with the submillimetre detection limits and any flux density measurements at shorter wavelengths in the FIR (e.g. at 70 μm or at 350 μm).

The FIR luminosity is then converted into a star formation rate (SFR) using the following relation:

$$\text{SFR}(M_{\odot} \text{ yr}^{-1}) = 1.7 \times 10^{-10} L_{\text{FIR}}(L_{\odot}) \quad (4)$$

from Kennicutt (1998). The inner quartile (25–75 per cent) of SFRs is 400–1600 $M_{\odot} \text{ yr}^{-1}$ with a median of 700 $M_{\odot} \text{ yr}^{-1}$. Both the derived quantities, L_{FIR} and SFR, are given in Table 3. We also derive UV-inferred SFRs using v -band and i -band optical photometry. Since all SFRGs are quite optically faint ($i > 22$) and FIR luminous, they are potentially subject to significant (yet uncertain) extinction factors. While not taken into account for the UV-inferred SFRs themselves, the large extinction factors may be deduced from the large disparities between $\text{SFR}_{\text{radio}}$ and SFR_{UV} given in Table 3 with a typical ratio of $\text{SFR}_{\text{radio}}/\text{SFR}_{\text{UV}} = 30$ (we do not consider $\text{SFR}_{\text{radio}}/\text{SFR}_{\text{UV}}$ to have AGN contamination based on the previous section).

Additional evidence that extinction caused by dust is significant comes out of the comparison between rest-UV morphologies and their MERLIN+VLA radio morphologies as seen in Fig. 5. Since the brightest and/or bluest components of the rest-UV emission and radio emission do not often coincide, it indicates that the dustiest, most FIR-luminous regions in the galaxy could be highly obscured.

Total SFR densities, Σ_{SFR} , are estimated by dividing these SFRs (from VLA fluxes) by the surface areas of MERLIN+VLA radio emission regions. We measure an effective star formation surface area by isolating the regions where MERLIN+VLA radio emission is significant to $>3\sigma$ (the values for effective radius of radio emission and SFR density, Σ_{SFR} , are given in Table 3). The median total SFR density is $30^{+40}_{-20} M_{\odot} \text{ yr}^{-1} \text{ kpc}^{-2}$. Note that this is potentially an overestimation of the SFR density since the radio flux contained within the $>3\sigma$ MERLIN+VLA region constitutes a fraction of the total VLA radio flux (it is inferred that this fraction is within 40–90 per cent). For this reason we also compute alternative SFR densities using the total integrated MERLIN+VLA flux within the $>3\sigma$ emission area. We convert the flux to a radio luminosity, then FIR luminosity, then SFR, and divide it by the area. The median value for this alternative SFR density is $10^{+20}_{-10} M_{\odot} \text{ yr}^{-1} \text{ kpc}^{-2}$ which is on average, three times less than the total Σ_{SFR} .

Comparing either SFR density measurements to their theoretical maximum – the maximum gas density divided by the local dynamical time (see equation 5 of Elmegreen 1999, we use $t_{\text{dyn}} = 4 \times 10^7 \text{ yr}$) – we can determine if the implied SFR density exceeds the theoretical prediction. While local ULIRGs with $\Sigma_{\text{SFR}} \approx 200 M_{\odot} \text{ yr}^{-1} \text{ kpc}^{-2}$ are forming stars at their theoretical maximum (e.g. Tacconi et al. 2006), only one of the SFRGs exceeds this limit, which is a dust opacity Eddington limit for SFR density (see Thompson, Quataert & Murray 2005). This source is RGJ123642, the highest redshift source in our sample having a low S/N in the radio, meaning the measured effective radius is unusually small. Even by assuming unresolved radio profiles, only

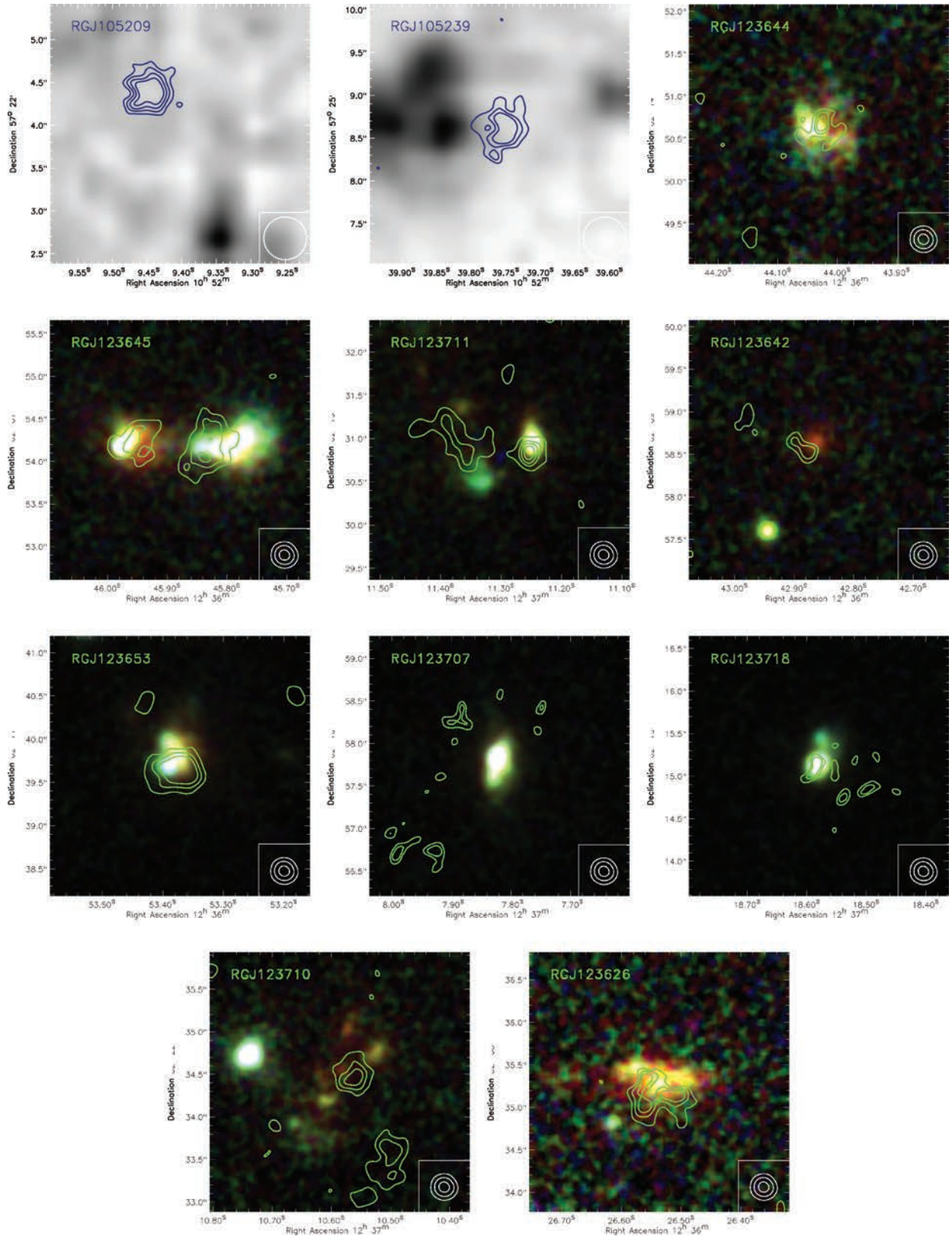


Figure 5. Contours of MERLIN+VLA high-resolution 0.4–0.5 arcsec radio emission overlaid on 3×3 arcsec² optical imaging for the CO-observed SFRGs. The optical imaging of GOODS-N sources is from *HST*-ACS *B*, *V* and *z* bands (presented in tricolour). The Lockman Hole sources have ACS *i*-band (black and white cutouts). The MERLIN+VLA beam shape is shown in the lower right of each panel in white (outer contour is the FWHM). The contour levels plotted integer multiples of σ starting at 3σ (except for RGJ123711 and RGJ123653, where only 3σ , 5σ and 7σ contours are shown for clarity). Structure in radio emission is seen in these galaxies on 1–8 kpc scales.

RGJ123642 exceeds the maximal starburst density, further highlighting that even starburst emission can dominate unresolved radio emission. In contrast, it would be unlikely for extended radio emission (this faint at these redshifts) to be driven by emission from AGN.

The star formation efficiency (SFE) can be calculated by dividing the FIR luminosity by the H_2 gas mass. This calculation is contingent on the gas reservoir being in the same region as the starburst, which is an assumption which needs to be investigated in more detail through future high-resolution multiple- J CO maps and resolved FIR emission maps. The mean SFE for SFRGs is $280 \pm 260 L_\odot M_\odot^{-1}$. Put another way, the median depletion time-scale (defined as M_{H_2}/SFR , assuming 100 per cent efficiency) for SFRGs is ~ 34 Myr with inner quartile 20–55 Myr. It should be noted here that a different gas conversion factor [e.g. $4.5 M_\odot (\text{K km s}^{-1} \text{pc}^2)^{-1}$] would increase the depletion time-scale and decrease the SFE by 5.6 times.

3.6 Dust temperature and dust mass

We fit FIR spectral energy distributions (SEDs) to the FIR flux density limits at 70, 350, 850 and 1200 μm (see Table 1 for details). Our fitting method follows the methodology of Chapman et al. (2004), Chapman et al. (2005) and Casey et al. (2009a): a single dust temperature modified blackbody fit. We fix the dust emissivity β to 1.5 and use the FIR/radio correlation to infer an FIR luminosity from the radio flux. Since we are limited by a lack of data in the FIR for most of our sample (many only have limits), our derived dust temperatures are not well constrained. However, if the uncertainty in our assumption of the radio/FIR correlation and dust emissivity are taken as givens, then we deduce temperature uncertainties on the order of 20–30 K. This is calculated by assuming L_{FIR} scales with L_{radio} ; a higher L_{radio} implies a high L_{FIR} , and a FIR SED with a high L_{FIR} can then be constrained by the FIR flux density measurements, even in the case of upper limits. Despite the large uncertainties, our measurements (whose statistical mean is 65 K) are consistent with a selection of warmer dust galaxies, even though there may be outliers.

We also estimate dust mass for the SFRG sample by using the following relation:

$$M_{\text{dust}}(M_\odot) \simeq \frac{S_{\text{obs}} D_L^2}{\kappa_\nu B(\nu_{\text{obs}}, T_d)}, \quad (5)$$

where κ_ν is the dust mass absorption coefficient as a function of rest wavelength: $\kappa_{850} = 0.15 \text{ m}^2 \text{ kg}^{-1}$, $\kappa_{250} = 0.29 \pm 0.03 \text{ m}^2 \text{ kg}^{-1}$ (Wiebe et al. 2009) and $\kappa_{70} = 1.2 \text{ m}^2 \text{ kg}^{-1}$ (Weingartner & Draine 2001). Again, the lack of FIR data means that our dust mass calculations are not well constrained; our SFRGs have a mean dust mass upper limit (at 2σ) of $\langle M_{\text{dust}} \rangle < 2 \times 10^9 M_\odot$, which is not a well-constrained measurement. A quick comparison to the mean gas mass ($2 \times 10^{10} M_\odot$) implies mean dust-to-gas ratios of $< 1/10$ (well within expectation).

3.7 Stellar mass

To estimate the galaxies' stellar masses, we combine the photometric points in the optical (*HST* ACS B , V , i and z for GOODS-N, *HST* ACS i for Lockman Hole and Subaru i for SSA13) and the mid-IR (*Spitzer*-IRAC 3.6, 4.5, 5.8 and 8.0 μm). For $z = 1$ –3, these photometric points cover rest frame 1.6 μm where stellar emission peaks. We use the *HYPERZ* photometric redshift code (Bolzonella, Miralles & Pelló 2000) to fit this photometry to several stellar population

SEDs (Bruzual & Charlot 2003). Using the best-fitting stellar population SED, we estimate the rest-frame H -band magnitude. While rest-frame K band is often used to measure stellar mass for high-redshift galaxies (using the method outlined by Borys et al. 2005), recent work has shown that stellar masses derived from K band are overestimated due to increased contribution from AGN power law and decreased contribution from star light at longer wavelengths (see Hainline et al. 2009). The mean light-to-mass ratio, L_H/M , can range from 5 to $10 L_\odot/M_\odot$, and using the Bruzual & Charlot (2003) models, is set at $5.6 L_\odot/M_\odot$ for SMGs as in Hainline et al. The mean rest-frame H -band absolute magnitude is -25.4 ± 0.8 with an inferred average stellar mass of $7 \times 10^{10} M_\odot$. These masses are consistent with the H -band derived SMG stellar masses (H -band absolute magnitude averages -25.8 ± 0.2 and masses average 2×10^{11}) found by Hainline et al. (2009) and a factor of ~ 2 lower than the K -band SMG masses derived by Borys et al. (2005).

Fig. 6 illustrates the best stellar population models with respect to the galaxies' photometric data. If an excess flux density is detected above the stellar model SED at the observed 8 μm then an AGN might be contributing significantly to the near-infrared luminosities (see Section 4.1 for an analysis of AGN contamination). While there are potential flux excess in seven of the 15 sources illustrated, the excess is only significant $> 2\sigma$ in RGJ123653 and RGJ123718. The former is discussed in detail in Casey et al. (2009a) who infer an insignificant AGN contribution based on combined evidence from X-ray (very low flux, consistent with starbursts), extended radio emission (inconsistent with AGN radio emission), and no clear power law dominating the near- to mid-IR data. The latter has extended radio emission, no X-ray detection and is the faintest radio galaxy of our sample ($\sim 15 \mu\text{Jy}$), and therefore, it is unlikely that it is dominated by a very powerful AGN. There is no clear relation between a system's stellar mass and its resulting detection in CO.

The galaxies' formation time-scales are given by $\tau_{\text{form}} \propto M_*/\text{SFR}$; the median τ_{form} of the sample is 10 Myr. While this quantity could be overestimated if M_* is overestimated, the formation time-scales likely represent a lower limit on the time it took to build up the stellar population since the SFRs are hypothetically near their peak during the ULIRG phase ($\gtrsim 200 M_\odot \text{ yr}^{-1}$) in comparison to most galaxies at the same epoch (1 – $10 M_\odot \text{ yr}^{-1}$). The hypothesis of SFRGs being near the peak is based on the fact that their SFRs are not sustainable beyond ~ 100 Myr, but it is unlikely that these systems are that young; it is more probable that SFRGs evolved more slowly, building up stellar mass gradually until a point, when a trigger led to an extreme starbursting phase.

4 DISCUSSION

Here we explore the relationship between the CO observations in SFRGs and their other multiwavelength properties, drawing on comparisons with other galaxy populations. CO observations provide a unique and independent probe of the galaxies' star formation properties, by constraining the molecular gas reservoirs which fuel the star formation. In Table 4 we have summarized many of the measured physical properties of SFRGs relative to SMGs for quick reference. It is important to note, however, that the SMGs of Table 4 are those with CO observations, limited to the mostly bright SMG subsample. After comparing with other populations, we discuss the implications that these observations have for the study of all high- z ULIRGs and how improved targeted observations, in both molecular interstellar medium lines and FIR continuum, will enable a thorough, unhindered analysis of ULIRG evolution and extreme star formation at $z \sim 2$.

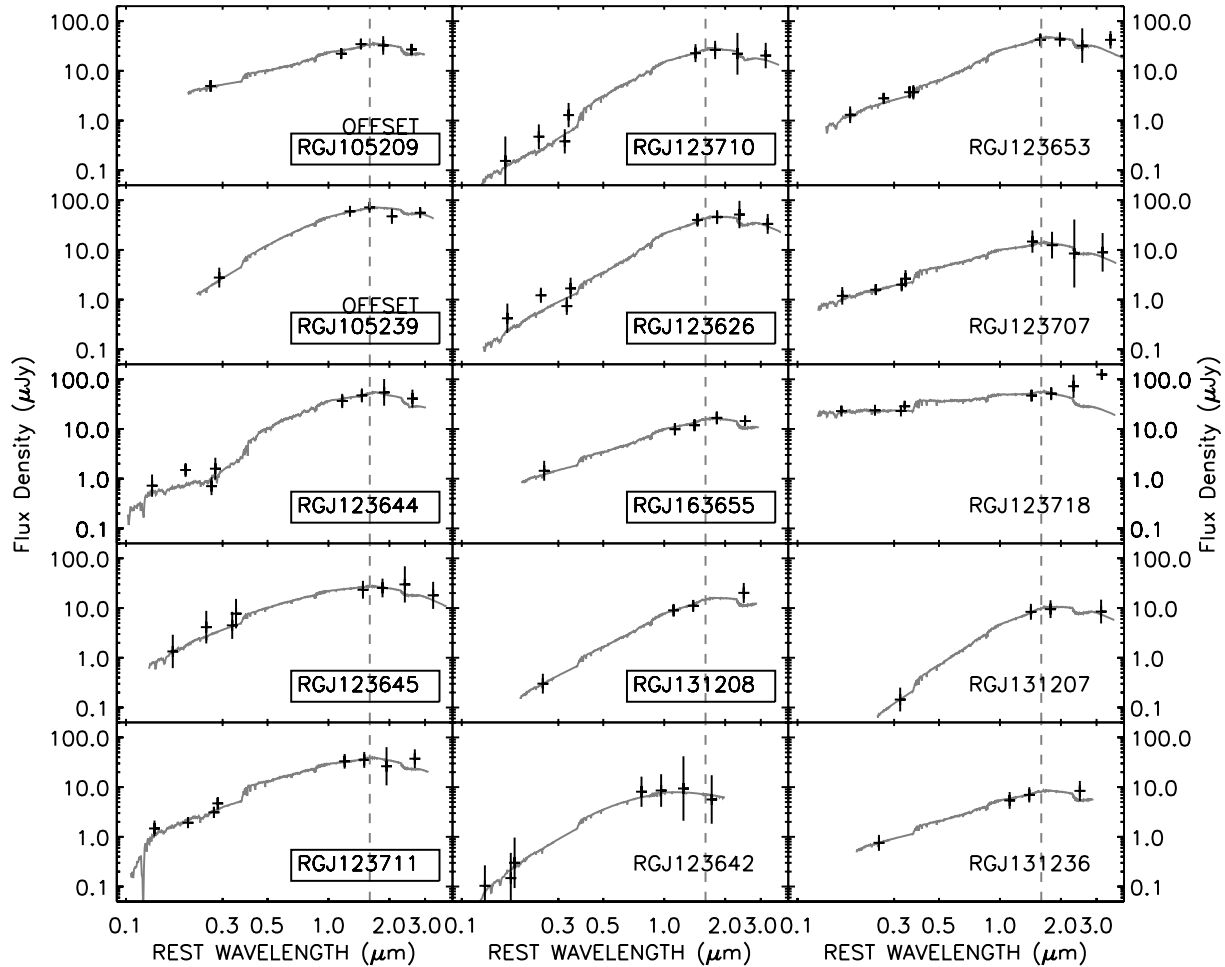


Figure 6. Stellar population models are fit to SFRG optical and near-IR photometric points. We estimate stellar mass using the rest-frame H -band magnitudes which are inferred from the fits; the method is described in Section 3.7. The SFRGs which are detected in CO have their names enclosed in boxes.

The original motivation for segregating submillimetre-faint and submillimetre-bright populations for CO observations is the premise that they exhibit similar extreme starburst qualities, thus molecular gas qualities, but differ in dust distribution whereby slightly warmer dust systems are undetectable at $850\ \mu\text{m}$ (the usual SMG-selection band). Surveying SFRGs in CO provides confirmation, through detection of vast gas reservoirs, that SMGs are not the only significant population of ULIRGs at high- z . The basic physical premise of the comparison is that the dust distribution in SFRGs would need to be clumpier or more compact to be heated to slightly higher dust temperatures. Since SFRG radio morphologies on average seem to be similarly extended and irregular, SFRGs are suggested to be less homogeneously diffuse than SMGs (Hainline et al. 2009; Menéndez-Delmestre et al. 2009), with more concentrated clumps, yet spread over the same large area.

4.1 Multiwavelength properties of SFRGs and AGN fraction

Table 3 provides a summary of SFRGs' physical properties derived from multiwavelength data. It includes AGN/starburst classifications for each individual SFRG, which help shed light on the complex nature of the population, and the potential for AGN contamination. 'Class^X' classifies SFRGs based on X-ray luminosity, 'Class^{IR}' classifies according to $8\text{-}\mu\text{m}$ flux excess in the near-IR,

and 'Class^{CO}' classifies according to FIR-to-CO luminosity ratio (where an unusually high ratio can be accounted for by an AGN contributing significantly to radio luminosity, thus overestimated FIR luminosity). A fourth class and fifth could also be defined, as rest-UV/optical spectroscopic features and as a function of the SFR density as traced by MERLIN+VLA morphologies; however, we have noted that all of the samples' morphologies are consistent with starbursts in both criteria. While we offer the reader the flexibility to interpret the AGN content of the SFRG sample as (s)he deems fit, we infer a total SFRG AGN fraction of 0.3 ± 0.1 to first order (included in Table 4), the mean AGN-dominated fraction from each of the three Table 3 classifications. This agrees with earlier measurements and estimates for SFRGs given in Casey et al. (2009b) and Casey et al. (2009a). Also, the possibility exists that a weak beaming of low-luminosity radio jets could overestimate radio luminosity by factors of a few for some SFRGs (please see Casey et al. 2009b, for the detailed discussion of radio beaming in more compact SFRGs). Again, we caution that AGN contamination has the potential to strongly bias the CO observations/interpretation of individual objects.

Fig. 5 shows that SFRGs have faint optical luminosities, suggestive of heavy reddening or obscuration by dust. This idea is supported further by the large discrepancy between SFRs derived from radio luminosity versus rest-UV flux densities. Even after

Table 4. SFRG properties summarized relative to SMGs.

Property	SFRGs	SMGs ^a
$\langle z \rangle$	1.8 ± 0.7	2.4 ± 0.6
$L_{\text{FIR}} (L_{\odot})$	$(4 \pm 3) \times 10^{12}$	$(8 \pm 4) \times 10^{12}$
SFR ($M_{\odot} \text{ yr}^{-1}$)	700 ± 500	1400 ± 500
$\langle R_{\text{eff}} \rangle$ (kpc) ^b	2.3 ± 0.8	2.7 ± 0.4
$\Sigma_{\text{SFR}} (M_{\odot} \text{ yr}^{-1} \text{ kpc}^{-2})^b$	30^{+40}_{-20}	60^{+140}_{-40}
$T_{\text{dust}} (K)^c$	66 ± 15	41 ± 5
$M_{\text{dust}} (M_{\odot})^c$	$< 2 \times 10^9$	9×10^8
H -band mag	-25.4 ± 0.8	-25.8 ± 0.2
$M_{\star} (M_{\odot})$	$(7 \pm 6) \times 10^{10}$	$(2 \pm 1) \times 10^{11}$
$\langle \tau_{\text{form}} \rangle$ (Myr)	10^{+15}_{-6}	14^{+8}_{-4}
$M_{\text{H}_2} (M_{\odot})$	$(2.1 \pm 0.7) \times 10^{10}$	$(5.1 \pm 2.8) \times 10^{10}$
$\Delta V_{\text{CO}} (km s^{-1})$	320 ± 80	530 ± 150
SFE (L_{\odot}/M_{\odot})	280 ± 260	450 ± 170
$M_{\text{dyn}} \sin^2 i (M_{\odot})^d$	$(7.2^{+6.8}_{-3.4}) \times 10^{10}$	$(1.5^{+1.4}_{-0.4}) \times 10^{11}$
$\langle \tau_{\text{depl}} \rangle$ (Myr)	34 ± 24	40^{+50}_{-30}
$f_{\text{gas}} = \langle M_{\text{gas}}/M_{\text{dyn}} \rangle^e$	$0.07^{+0.11}_{-0.02}$	$0.09^{+0.09}_{-0.07}$
$f_{\text{stars}} = \langle M_{\star}/M_{\text{dyn}} \rangle^e$	~ 0.2	~ 0.3
$f_{\text{CO}(4-3)/\text{CO}(3-2)}^f$	2.0 ± 0.8	1.4 ± 0.2
f_{AGN}^g	0.3 ± 0.1	0.4 ± 0.2

^a All aggregate properties of SMGs are measured with respect to the CO-observed subset from Neri et al. (2003), Greve et al. (2005) and Tacconi et al. (2006).

^b Effective radius and SFR density are measured for MERLIN+VLA imaged SFRGs only. The effective size of SMGs is from Biggs & Ivison (2008) and the SFR density is the SMG SFR divided by the mean R_{eff} .

^c T_{dust} and M_{dust} fits for SFRGs are described in Section 3.6; while both measurements are highly uncertain due to poor FIR flux density constraints, their calculation is useful for comparison with SMGs from Chapman et al. (2005) and Kovács et al. (2006).

^d Dynamical mass assumes an effective radius of 2 kpc for SFRGs and SMGs without radio size measurements; for SMGs, this size is supported by measurements from Tacconi et al. (2008), and for SFRGs the size has been shown to be similar for one SFRG (Bothwell et al. 2010) and is similar to their MERLIN+VLA radio sizes (R_{eff}).

^e The gas and stars fraction represent the fraction of total mass which is in gas (or in stars), internal to each galaxy. Note that the gas fraction does not include the 40 per cent correction for helium.

^f The ratio of CO line fluxes represents the source excitation. The value for SFRGs is based on the single measurement of RGJ123711 described in Section 3.2, and the SMG measurement is taken from the three SMGs measured by Weiss et al. (2007).

^g The AGN fraction (within a population) is estimated in the SFRG sample as described in Section 4.3, while the AGN fraction of CO-observed SMGs is taken from their rest-UV spectral classification (note that none of the SFRGs has AGN spectral signatures). The entire SMG population is estimated to have an AGN fraction of ~ 0.25 (see Alexander et al. 2005).

correction for dust extinction using the UV slope and dust extinction models of Calzetti, Kinney & Storchi-Bergmann (1994), the UV-derived SFR can be a factor of 10–100 lower than the radio-inferred SFR demonstrating that SFRGs are far dustier than normal dust extinction laws predict (which also holds for SMGs). Their radio morphologies are primarily extended and irregular, thus attributable to star formation and not compact AGN as is also the case for SMGs (Chapman et al. 2004; Biggs & Ivison 2008). We also note the effective MERLIN+VLA radii between SFRGs that have been CO-detected ($R_{\text{eff}} = 2.7 \pm 0.6$ kpc) and those that have not ($R_{\text{eff}} = 1.7 \pm 0.8$ kpc). While the difference is insignificant, it could be explained by observing that the sources with lower effective radii have lower S/N in the radio, implying lower FIR luminosities.

If we assume the inferred radio/FIR and the ULIRG $L'_{\text{CO}}/L_{\text{FIR}}$ relations, we predict integrated CO fluxes of $0.1\text{--}0.3 \text{ Jy km s}^{-1}$ for CO-undetected sources based on radio flux density (requiring particularly sensitive observations with our set-up).

Fig. 6 showed that most SFRGs have only minor AGN contribution in the near-IR; most emission is dominated by stars. The stellar masses of SFRGs average $7 \times 10^{10} M_{\odot}$, consistent with SMG masses derived by Hainline et al. (2009) using the rest H -band luminosity but a factor of $\sim 2 \times$ lower than the SMG masses of Borys et al. (2005) from the rest K -band luminosity.

4.2 Comparing to SMGs

The comparison of molecular gas properties between SFRGs and SMGs is the main focus of this work; however, a strong selection bias is folded into this comparison. The first SMGs to be observed in CO (Neri et al. 2003; Greve et al. 2005; Tacconi et al. 2006) were among the brightest SMGs with spectroscopic redshifts ($L_{\text{FIR}} \gtrsim 10^{12.5} L_{\odot}$) since brighter L_{FIR} systems had a higher likelihood of being CO detected. We note that the luminosity distribution of SMGs plotted in Fig. 1 includes many lower luminosity SMGs which have recently been observed in CO, in parallel to our SFRG observing programmes, but have not yet been analysed or published (Bothwell et al., in preparation). Most of the ‘bright-SMGs’ (those with published CO spectra) have AGN signatures in their rest-UV spectra, a property that would exclude them from SFRG selection if they were submillimetre-faint. This means that similarly bright radio sources which are submillimetre-faint, comparable to the ‘bright-SMGs,’ were excluded from our sample due to AGN contamination.

Besides the luminosity bias introduced by weeding out AGN as revealed by rest-UV/optical spectroscopy, a further bias exists due to spectroscopic incompleteness of the SFRG population. Since their radio emission was more likely thought to be dominated by AGN, SFRGs were not followed up in rest-UV/rest-optical spectroscopy nearly as thoroughly or completely as SMGs. This likely means that the absolute brightest SMGs were CO observed while a large sample of bright SFRGs could have been excluded from CO observations due to a lack of reliable redshift information or potentially strong AGN contamination. Furthermore, the original SFRG selection of Chapman et al. (2004) had the added criteria of a faint optical magnitude $i > 23$, which made redshift measurement from rest-UV spectra more difficult. There has been some anecdotal indication, however, that warmer dust systems might not exist at the highest luminosities with the same frequency as colder dust systems, as revealed by 250 μm selected HyLIRG populations (Casey et al. 2011).

We note that the misidentification of optical counterparts to SMGs has potentially led to a lower CO-detection rate for that population than other CO-observed galaxy populations; some of the radio galaxy SMG-counterparts might not be starbursts and might have intrinsically low FIR luminosities, thus CO luminosities. We note that SFRGs (although not faced with the issue of matching FIR positions to a correct radio counterpart) could also suffer from the selection of non-starburst radio galaxies.

In the sections below, we frequently discuss how SFRGs relate to SMGs: both the CO-observed ‘bright’ subsample of SMGs and extrapolations based on preliminary analysis on the fainter, more numerous sample of SMGs (Bothwell, private communication). The overall luminosity bias existing in these distinct samples must be kept in mind when population comparisons are made.

4.3 Star formation efficiencies

The relationship between SFR and molecular gas mass is paramount to a galaxy's evolutionary interpretation. This is measured by comparing the FIR luminosity with CO line luminosity, as we show in Fig. 7. In this context, SFRGs appear to have similarly high CO luminosities as SMGs, and most SFRGs lie slightly above the 'ULIRG' SFE power-law relation, $L'_{\text{CO}} \propto L'_{\text{FIR}}{}^{0.61}$, which is followed by both local ULIRGs and SMGs. However, SFRGs are inconsistent with the SFE relation which describes local spiral galaxies ($L'_{\text{CO}} \propto L_{\text{FIR}}{}^{0.93}$; Solomon & Sage 1988; Gao & Solomon 2004). The SMGs shown in Fig. 7 are those of Neri et al. (2003), Greve et al. (2005) and Tacconi et al. (2006). As mentioned in Section 4.2, SFRGs are a factor of ~ 2 less luminous in radio (thus L_{FIR}) than CO-observed SMGs. Due to their relative high luminosities with respect to local ULIRGs, the SMGs have been described as the *scaled-up* high-redshift analogues to local ULIRGs (Tacconi et al. 2006). In contrast, SFRGs probe a luminosity regime $\lesssim 10^{12.5} L_{\odot}$ closer to the locus of local ULIRGs at $\sim 10^{12} L_{\odot}$. While SFRGs might seem to be better analogues of local ULIRGs than SMGs in luminosity space, we note that the stellar and gas properties of the two populations are quite distinct: local ULIRGs being more compact with lower stellar masses than SFRGs and SMGs (Dasyra et al. 2006), and they have lower CO luminosities by a factor of $\sim 2-3$.

The SFEs of SMGs and SFRGs span the range of $70-1000 L_{\odot} M_{\odot}^{-1}$. The median SFE of the CO-detected SFRG sample is $280 \pm 260 L_{\odot} M_{\odot}^{-1}$ which is statistically consistent with the mean SFE for SMGs, $450 \pm 170 L_{\odot} M_{\odot}^{-1}$, although both values incorporate the large uncertainties of the gas conversion factor and FIR-derived SFR. Chapman et al. (2008) highlights that the two pilot programme $^{12}\text{CO}(J=3 \rightarrow 2)$ detections of RGJ123711 and RGJ163655 have exceptionally high SFEs and hypothesized that SFRGs, with further observation, might show similarly high SFEs compared to SMGs. Daddi et al. (2008) analysed the CO content of

two BzK selected galaxies (RGJ123710 and RGJ123626, also selected as SFRGs and included in our analysis) and claimed that they had relatively low, Milky Way/'normal spiral' efficiencies, emphasizing the difference between them and the high-efficiency ULIRGs. Our large sample of SFRGs, including both the Chapman et al. and Daddi et al. subsamples, reveals a much wider spread in SFEs, suggestive of a wide range in gas states and a possible range of galaxy states, although more SFRGs are consistent with the less-efficient Daddi et al. sample.

The SFRGs not detected in CO and those far below the ULIRG $L_{\text{FIR}}/L'_{\text{CO}}$ relation would appear to be very efficient star formers (less gas to fuel their high SFRs); however, this assumes that AGN contamination is minimal. AGN contamination is more likely than superefficient star formation and happens when AGN boosts the radio-inferred FIR luminosity, thus inferred SFR; as the empirical relation between L_{FIR} and L'_{CO} suggests, AGN-contaminated sources would be fainter in CO gas than predicted. We then can classify SFRGs in terms of CO luminosity to FIR luminosity (i.e. the ratio of $L'_{\text{CO}}/L_{\text{FIR}}$), where low ratios are designated 'AGN' in 'CLASS_{CO}' in Table 3. While the scatter of local ULIRGs around the $L'_{\text{CO}}/L_{\text{FIR}}$ relation is minimal, ~ 0.3 dex, both SFRG and SMG populations have more significant scatter below the relation; this is consistent with many SFRGs and SMGs having powerful AGN which boosts radio (thus FIR) luminosity.

The scatter of SFRGs above the ULIRG $L'_{\text{CO}}/L_{\text{FIR}}$ relation is suggestive of low SFEs as presented by Daddi et al. (2008) and Daddi et al. (2010). We caution that sources like RGJ123710 and RGJ123626, which have these low SFEs, it might be more appropriate to assume that the gas properties are more similar to spiral/disc galaxies than ULIRGs, particularly when converting to molecular gas mass using the CO/H₂ conversion factor. This factor differs greatly between ULIRGs [$0.8 M_{\odot}/(\text{K km s}^{-1} \text{pc}^2)$] and Milky Way type disc galaxies [$4.5 M_{\odot}/(\text{K km s}^{-1} \text{pc}^2)$]. Since the inferred gas masses differ so greatly given these different assumptions, we give M_{H_2} for both ULIRG and spiral/disc galaxy assumptions in Table 3

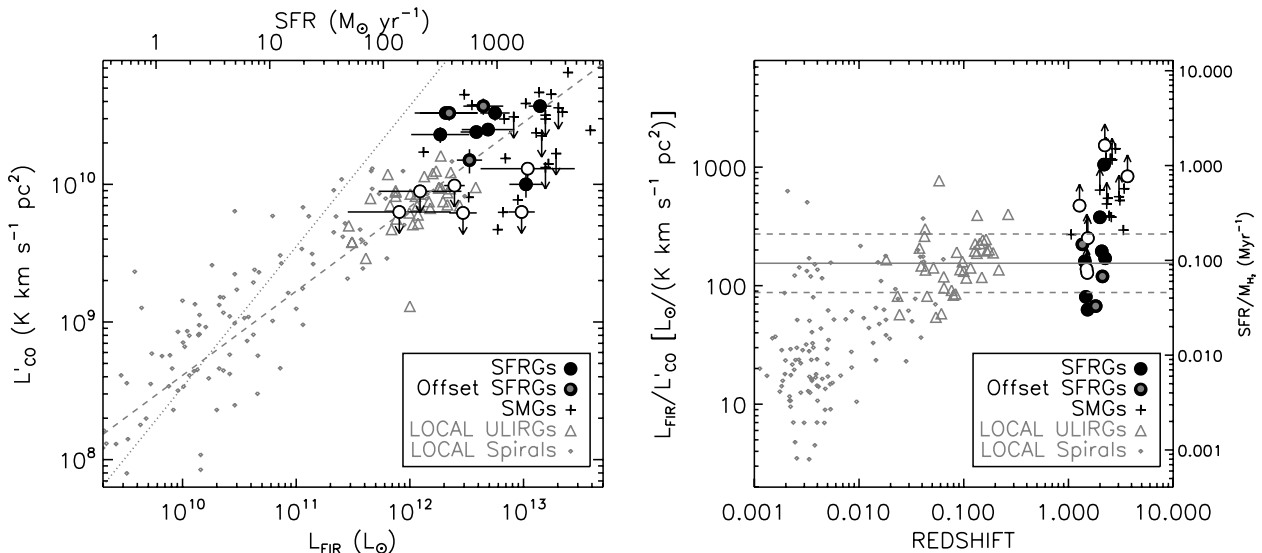


Figure 7. Left: FIR luminosity against CO luminosity, $L'_{\text{CO}[1-0]}$. SFRGs (black circles) lie in the same luminosity space as local ULIRGs (grey triangles; Solomon et al. 1997), while SMGs (crosses; Greve et al. 2005) have higher luminosities. SFRGs detected in CO are solid while SFRGs without CO detection are open circles. The tentative identifications or 'offset' CO sources are circles with grey centres. We also overplot data of spiral galaxies for perspective (grey diamonds; Solomon & Sage 1988; Gao & Solomon 2004), and include the best-fitting observed relations between L_{FIR} and L'_{CO} for local spirals (dotted line) and local ULIRGs/SMGs (dashed line). Right: the star formation efficiency, given by $L_{\text{FIR}}/L_{\text{CO}}$, is plotted with redshift. SFRGs appear to share the same range of SFEs as SMGs despite their fainter luminosities. The mean SFE and 1σ bounds of local ULIRGs are illustrated by the horizontal solid and dashed lines.

but proceed with our interpretation using the ULIRG conversion factor.

4.4 Linewidths: implications for merger stage

The distribution in CO linewidths provides an important insight into the galaxies' dynamics. Fig. 8 shows the ΔV_{CO} full width at half-maximum (FWHM) distributions for our SFRGs, SMGs (both 'bright' SMGs and the fainter sample observed in CO only recently; Smail, private communication) and local ULIRGs (Solomon et al. 1997). None of the linewidths presented here has made any inclination angle assumptions. The linewidths of SMGs were adjusted to correct for the prior exclusion of double-peaked Gaussians (see the details of this correction in Coppin et al. 2008); this reduced the mean SMG linewidth from 600 to 530 km s^{-1} . Despite the adjustment, SMGs seem quite distinct from SFRGs and local ULIRGs by having a high-FWHM tail in its distribution. This high-FWHM tail is seen only in a bright subsample of SMGs originally surveyed in CO gas. While it could be attributed to selection bias, in that wide CO features are only detectable in the brightest objects where S/N is much higher, we highlight that there was significant improvement in receiver sensitivity between observations of these bright and wide SMG CO lines and the fainter SFRG observations, so the data have comparable S/N. This raises the possibility that only the brightest subsample of high- z ULIRGs ($L_{\text{FIR}} \gtrsim 10^{13} L_{\odot}$) have wide CO linewidths ($\gtrsim 500 \text{ km s}^{-1}$).

Broad dispersion-dominated CO lines (and irregular double-peaked profiles) in the highest luminosity systems is suggestive of early-stage major mergers where two gas-rich discs are infalling. Local ULIRGs in contrast have a much narrower linewidth distribution and are a factor of ~ 5 – 10 fainter in L_{FIR} . For this reason, local ULIRGs are often said to be in a late starburst phase, at a coalesced point during a merger (when progenitors have coalesced into a single system; for a review see Sanders & Mirabel 1996). SFRGs and more modest luminosity SMGs are difficult to place

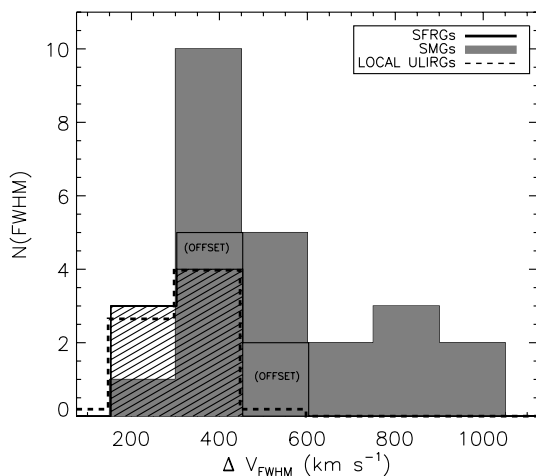


Figure 8. The distribution in CO linewidths for the SFRG sample compared to local ULIRGs (Solomon et al. 1997) and SMGs. The offset/tentative SFRGs (open histogram) are added on top of the remaining SFRG sample (hashed area). The distribution for local ULIRGs has been renormalized with respect to the total number of SFRGs for a more clear comparison. The SMG distribution has been corrected for overestimation in linewidths which is caused by fitting a single Gaussian to a double-peaked CO line, and the SMG distribution includes the samples of Neri et al. (2003), Greve et al. (2005) and Tacconi et al. (2006), as well as some yet unpublished SMG observations (Bothwell et al., in preparation).

in this evolutionary sequence, but their populations are not likely to be exclusively dominated by either beginning or ending merger substages.

The lower dynamical masses of local ULIRGs (typical sizes $R = 1 \text{ kpc}$ and $\Delta V = 300 \text{ km s}^{-1}$) could be due to downsizing – where extreme starbursts today are less massive than those at high- z . Both SFRGs and SMGs are consistent with this picture since they seem to be a factor of ~ 2 larger ($R_{1/2} \gtrsim 2 \text{ kpc}$; see measurements of CO size in Tacconi et al. 2008; Bothwell et al. 2010; Daddi et al. 2010). The subsample of SMGs that have very broad features may be in a particular stage of merger where their line profile becomes broadened, perhaps in observation of two distinct components with very small physical separation or gas. This would appear to increase our dynamical mass estimates of these systems. However, the radial ‘size’ and merger correction factor C would both need to be reassessed (both of which have not been measured on a case-by-case basis for these sources) before physical interpretation of higher dynamical mass estimates are made.

Although more observations need to be taken to conclude, an alternative explanation for the narrower linewidths observed in modest-luminosity sources, including SFRGs, is that the population consists of fewer major mergers than the very bright systems. Observational evidence indicates that anywhere from 50 to 90 per cent of local ULIRGs have undergone recent mergers (e.g. Lawrence et al. 1989; Melnick & Mirabel 1990; Clements et al. 1996), but that a sizable fraction might be triggered by other mechanisms. Recent work from Genzel et al. (2008) suggests that high SFRs in secularly evolving disc galaxies may be caused by rapid rotation or smooth accretion of material from its surroundings (e.g. minor merging or tidal accretion). In addition, theoretical work indicates that the high SFRs and IR luminosities in ULIRGs could often be generated by minor mergers and turbulent disc processes (e.g. Monaco 2004; Dib, Bell & Burkert 2006). ULIRGs driven by secular processes would exhibit narrow CO linewidths, consistent with the SFRGs presented in this paper. High spatial resolution gas observations are needed to determine the true nature of their dynamics, however.

Recent observations and simulation work have reiterated the idea that $>10^{13} L_{\odot}$ ULIRGs are more often in early-stage major mergers. Tacconi et al. (2008) and Engel et al. (2010) show that most SMGs at $z \sim 2$ exhibit disturbed gas morphologies rather than smoothly rotating discs, and simulations and semi-analytic SMG models tell us that major mergers likely initiate most ultraluminous phases of high- z star formation seen in SMGs (Baugh et al. 2005; Swinbank et al. 2008; Narayanan et al. 2009). However, recent work from Davé et al. (2010) indicate that ULIRGs may also be driven by continual bombardment by very low mass fragments on to a $\sim 10^{11} M_{\odot}$ galaxy. Cold streams feeding continual gas build-up (e.g. Dekel et al. 2009) has also been raised as a possible origin. The tail of large CO linewidths in SMGs provides a crucial piece of observational evidence that some SMGs are much more highly disturbed and represent a different phase than SFRGs and local ULIRGs.

We note that the mean gas fraction, defined as gas mass to dynamical mass ratio, of SFRGs, is $\langle M_{\text{gas}}/M_{\text{dyn}} \rangle = f_{\text{gas}} = 0.07^{+0.11}_{-0.02}$, consistent with the same ratio for SMGs, which have $\langle M_{\text{gas}}/M_{\text{dyn}} \rangle \sim 0.09^{+0.09}_{-0.07}$ (after correction for a 30° inclination angle). While this comparison is between SFRGs which have lower luminosities than CO-observed SMGs, the same molecular gas fraction suggests that the two populations are likely in similar evolutionary stages. We note, however, that if we assume a CO/H₂ gas conversion factor consistent with spirals instead of ULIRGs, the gas mass fraction increases substantially to ~ 0.60 . While overall, SFRGs and SMG properties are more consistent with ULIRGs, it is possible that

a few outliers, for example RGJ123710 and RGJ123626 described in (Daddi et al. 2008) and a few of the SMGs exhibiting unusually low SFEs, are much more gas rich than the ULIRGs which comprise the rest of the populations.

4.5 Comparison with other populations

An evolutionary transition stage between ULIRG and quasar has been explored extensively by work on dust obscured galaxies (DOGs; Dey et al. 2008; Pope et al. 2008), a population of galaxies with warm dust temperatures and more modest SFRs than the brightest SMGs, consistent with $\sim 10^{12} L_{\odot}$ ULIRGs. 10 of 14 SFRGs with 24- μm flux measurements satisfy DOG selection. While DOG selection is quite broad and selects nearly all SFRGs and many SMGs (requiring 24- μm flux densities $> 100 \mu\text{Jy}$ and red optical to IR colours), a subset of DOGs with spectroscopic redshifts have detailed near-IR to FIR photometric constraints (Bussmann et al. 2009) which show that AGN may contribute significantly to their bolometric luminosities, and as a result, most have warm dust temperatures ($T_d \gtrsim 45$ K). Due to their high AGN fraction (dependent on luminosity and only $\ll 0.5$ in the faintest, $S_{24} < 0.5$ mJy subset, e.g. Pope et al. 2008) and heavy dust obscuration, many DOGs are believed to lie at the transition phase between SMGs (or star-forming ULIRG) and luminous quasar (Pope et al. 2008) and overlap with the SFRG population.

While SFRGs might have warm dust temperatures like some DOGs, we find that most are dominated by star formation and not AGN. This is largely a function of the aggressive selection of SFRGs, meant to weed out strong AGN by their spectral indicators in the rest-UV/optical and the observation of a minimal 8- μm flux excess and of an extended radio emission. High SFRs and a low AGN fraction (with respect to a higher AGN fraction in DOGs) are strong evidence that SFRGs are at a similar ULIRG phase to SMGs despite their warm dust.

The molecular gas fractions of $z \sim 2$ normal starburst galaxies have been estimated at $f_{\text{gas}} \sim 0.4\text{--}0.5$ (assuming a $L_{\text{CO}}/L_{\text{FIR}}$ prior; Erb et al. 2006). The gas fraction in SMGs (and a few BX active galaxies) has been measured to be $f_{\text{gas}} \sim 0.3\text{--}0.5$ (these values do not take inclination into account, which is a factor of 1/4, Tacconi et al. 2008). We measure an internal gas fraction of our SFRG sample of ~ 0.07 , which is consistent with SMGs, both the Tacconi et al. estimate ($f_{\text{gas}} \sim 0.1$ if corrected for inclination) and our reassessment of the same data ($f_{\text{gas}} = 0.09_{-0.06}^{+0.08}$). All the f_{gas} measurements for high- z ULIRGs ($f_{\text{gas}} \sim 0.1$) are lower than the inferred gas fractions for normal $z \sim 2$ galaxies ($f_{\text{gas}} \sim 0.5$) from Erb et al. (2006). This could indicate that the more modest luminosity galaxies, consisting of gas-rich discs, have low dynamical masses but a proportionately high gas mass, meaning they would be good progenitor candidates for ULIRG systems, if set on collision courses with other gas-rich discs. During the ULIRG starburst phase, the gas mass would start to decrease with rapid star formation. In contrast, we recognize that by using a higher X_{CO} conversion factor more consistent with quiescent discs, then the measured gas fractions of these ULIRGs would increase by $\sim 6\times$, making their gas fractions consistent with those of the estimate for normal $z \sim 2$ galaxies. Future observations of more modest luminosity galaxies in CO gas (e.g. the recent work of Tacconi et al. 2010) are needed to truly understand the sequencing and gas properties of ULIRGs and their progenitors.

Fig. 9 highlights the unusually high SFRs per unit mass of SFRGs and SMGs above normal starbursts (AEGIS samples; Noeske et al. 2007), for a wide range of stellar masses. The relation between stellar mass and specific star formation rate has been shown to evolve

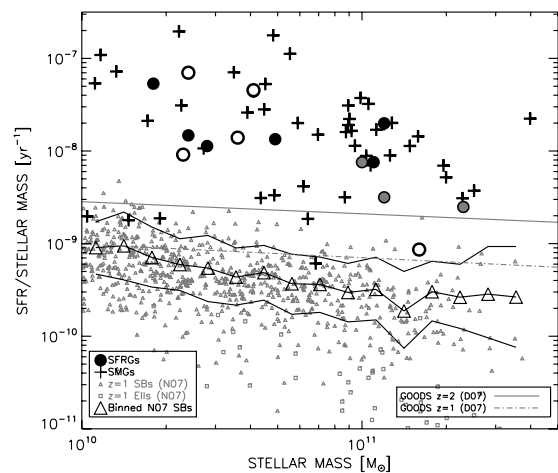


Figure 9. The star formation rate per unit stellar mass against stellar mass. We compare SFRGs (large circles) to SMGs (crosses) and $z \sim 1$ starburst galaxies (grey triangles and squares; Noeske et al. 2007). We also overplot the derived redshift-dependent relations (at $z = 1$ and $z = 2$, dot-dashed lines) found for GOODS galaxies in Daddi et al. (2007). SFRGs not detected in CO are open circles while detected SFRGs are filled. Like SMGs, SFRGs have very large star formation rates per stellar mass compared with ‘blue sequence’ galaxies, although their mean stellar mass ($\sim 7 \times 10^{10} M_{\odot}$) is less than the mean SMG stellar mass ($\sim 2 \times 10^{11} M_{\odot}$).

with redshift, e.g. Daddi et al. (2007); however, SMGs and SFRGs still lie at higher SFRs than galaxies of equal mass at the same redshift (e.g. da Cunha et al. 2010). This enhanced SFR fraction per unit mass reveals that SFRG and SMG star formation processes seem fundamentally different from SF processes in more modest luminosity galaxies, despite the overall range of stellar mass spanning almost 2 orders of magnitude.

The BzK active galaxy selection (Daddi et al. 2004) is meant to select moderate star forming ($\sim 100\text{--}200 M_{\odot} \text{ yr}^{-1}$), massive ($\sim 10^{11} M_{\odot}$) galaxies at high redshift – systems that are typically below the ULIRG SFR threshold ($\gtrsim 200 M_{\odot} \text{ yr}^{-1}$). Daddi et al. (2010) detect several active BzK galaxies in $^{12}\text{CO}(J = 2 \rightarrow 1)$ with surprisingly high gas masses given their SFRs, indicating that they exhibit gas properties more consistent with normal Milky Way type galaxies, but at ‘scaled-up’ luminosities, stellar masses and gas masses. It is important to note however that the active BzK galaxies observed in CO were all radio-detected, in other words, most of them have SFRs above the ULIRG cut-off ($> 200 M_{\odot} \text{ yr}^{-1}$) and might otherwise be characterized as SMGs or SFRGs. All SFRGs in this paper satisfy the active BzK selection criterion, indicating that BzK selection might probe both massive star-bursting galaxies and massive, extreme, dusty starbursts. Similarly, it appears as if SFRG selection might select both high- z ULIRG merging systems and extremely gas-rich disc galaxies.

4.6 Volume density

It is probable that the luminosity bias described in Section 4.2 has significant effect on how we can interpret the CO observations of either population.

Spectroscopic incompleteness in the SFRG population (as discussed in Section 4.2) makes volume density difficult to calculate. We estimate that about 35 per cent of a complete sample of μJy radio galaxies ($\sim 0.7 \text{ arcmin}^{-2}$) with $S_{1.4} > 20 \mu\text{Jy}$ have not been observed spectroscopically (see Chapman et al. 2003). The majority of these are submillimetre faint (since most spectroscopic observations of

μJy radio galaxies have been of SMGs). Of the submillimetre-faint galaxies which were spectroscopically observed, 65 per cent have confirmed redshifts, roughly half of which are low-luminosity AGN and the other half are star-forming galaxies. This means that by completing spectroscopic observations of known submillimetre-faint μJy radio galaxies in well-surveyed fields, the source density of star-forming, submillimetre-faint ULIRGs with redshifts would likely increase by ~ 30 per cent, increasing the source density of all high- z ULIRGs by $\gtrsim 15$ per cent, which could also increase the ULIRG contribution (including SMGs) to the cosmic SFR density at its peak (e.g. see Bouwens et al. 2009; Goto et al. 2010).

Future observations from SCUBA2 and the *Herschel Space Observatory* in the 50–500 μm range will dramatically improve the census of warmer dust ULIRGs (and all dusty starburst galaxies) at $z \sim 2$ through continued discovery, thus allowing a more thorough follow-up of the submillimetre-faint (and 50–500 μm bright) radio sample. With improved interferometric millimetre-line observations at low and high frequencies from the Atacama Large Millimeter Array (ALMA), we will be able to target these high-redshift sources in multiple CO transitions, thus removing an observational bias towards certain J -transitions of CO and enabling a more accurate calculation of gas masses. Without such strong temperature biases in gas and dust observations, a more complete interpretation of high-redshift ultraluminous galaxies will finally be possible.

5 CONCLUSIONS

We have presented CO molecular gas observations of a sample of submillimetre-faint SFRGs. Due to their non-detection at submillimetre wavelengths and lack of dominant AGN, these ultraluminous, μJy radio galaxies are thought to be dominated by star formation but have warmer dust temperatures than SMGs. Out of the 16 CO-observed SFRGs (12 from this paper and four from the literature), 10 are detected with a mean CO luminosity of $L'_{\text{CO}(1-0)} \sim 2.6 \times 10^{10} \text{ K km s}^{-1} \text{ pc}^2$, which is slightly less than that of the CO-observed SMG sample, despite being $\sim 2 \times$ less luminous in the radio. We attribute the luminosity difference to a selection bias but suggest that physical driving mechanisms might differ between the very bright ($> 10^{13} L_{\odot}$) and moderately bright ($\sim 10^{12} L_{\odot}$) populations.

High-resolution radio imaging from MERLIN+VLA shows that the radio emission in the SFRG sample is resolved and extended with mean effective radii $\sim 2 \text{ kpc}$, suggesting that the SFRG radio luminosities are dominated by star formation rather than AGN. The MERLIN+VLA size constraints are consistent with similarly analysed SMG MERLIN+VLA sizes. While we note that AGN do not dominate our sample, it is possible that several of our sources have non-negligible AGN due in part to their selection as radio galaxies. Due to limited FIR data, we use the FIR/radio correlation to derive L_{FIR} and then compute extinction-free SFRs from the FIR.

The SFEs of SFRGs are comparable within large uncertainties to those of SMGs and local ULIRGs, even though a few sources appear to have very high SFEs (like those in Chapman et al. 2008) or very low SFEs (like those in Daddi et al. 2008). Those with perceived very high SFEs are more likely AGN-dominated than superefficient; their FIR luminosities as calculated from the radio are probably overestimated.

SFRGs have narrower CO linewidths than the bright subsample of SMGs at the same redshifts ($\Delta V_{\text{SFRG}} \sim 320 \text{ km s}^{-1}$ and $\Delta V_{\text{SMG}} \sim 530 \text{ km s}^{-1}$), suggesting that SFRGs might have less disturbed dynamical environments. The linewidth distribution is potentially suggestive of different evolutionary stages or processes

between SFRGs and SMGs; however, the observed difference with SMGs could be due to an S/N or a luminosity bias. The former would mean that intrinsically broad lines would have underestimated FWHMs due to low S/N. The latter is due to the more thorough spectroscopic sampling of the SMG population. SMGs have higher spectroscopic completeness and they also include many objects with AGN signatures in the rest-UV/optical. Any SFRGs that have similar AGN signatures were culled from the sample, thus eliminating some of the potentially brightest SFRGs (most of the bright SMGs which have been surveyed in CO contain optical AGN). While less luminous SMGs (at the same luminosities of SFRGs) exist, few have been observed in CO, thus it is difficult to rule out that CO luminosity might relate to the distribution in CO with linewidth.

Despite selection biases, we have explored the possible physical scenarios triggering warm-dust ULIRGs in contrast to the well-studied cold-dust ULIRGs. SFRGs appear to bridge the gap between the properties of $> 10^{13} L_{\odot}$ SMGs and $\sim 10^{12} L_{\odot}$. Quantitatively, their extended radio emissions suggest sizes consistent with SMGs, implying much larger dynamical masses than local ULIRGs. We show that SFRGs have the same AGN fraction as SMGs and are therefore unlikely to represent a ‘post-SMG’ AGN turn-on phase. Luminous SMGs have been characterized as an early infall stage during a major merger, and local ULIRGs are often described at late-type major mergers. Here, we suggest that SFRGs (and less luminous SMGs) span the range of states during peak merger interactions.

ACKNOWLEDGMENTS

We thank the anonymous referee for detailed, helpful comments which helped improve this paper greatly. This work is based on observations carried out with the IRAM Plateau de Bure Interferometer. IRAM is supported by INSU/CNRS (France), MPG (Germany) and IGN (Spain). We acknowledge the use of GILDAS software (<http://www.iram.fr/IRAMFR/GILDAS>). This work is also based, in part, on observations by the University of Manchester at Jodrell Bank Observatory on behalf of STFC, and the VLA of the National Radio Astronomy Observatory, a facility of the National Science Foundation operated under cooperative agreement by Associated Universities, Inc. CMC thanks the Gates Cambridge Trust for support, IRS thanks STFC for support, and KC is supported by an STFC Postdoctoral Fellowship. Support for this work was provided by NASA through Hubble Fellowship grant *HST-HF-51268.01-A* awarded by the Space Telescope Science Institute, which is operated by the Association of Universities for Research in Astronomy, Inc., for NASA, under contract NAS 5-26555.

REFERENCES

- Alexander D. M. et al., 2003, *AJ*, 126, 539
- Alexander D. M., Bauer F. E., Chapman S. C., Smail I., Blain A. W., Brandt W. N., Ivison R. J., 2005, *ApJ*, 632, 736
- Baugh C. M., Lacey C. G., Frenk C. S., Granato G. L., Silva L., Bressan A., Benson A. J., Cole S., 2005, *MNRAS*, 356, 1191
- Biggs A. D., Ivison R. J., 2006, *MNRAS*, 371, 963
- Biggs A. D., Ivison R. J., 2008, *MNRAS*, 385, 893
- Blain A. W., Smail I., Ivison R. J., Kneib J., Frayer D. T., 2002, *Phys. Rep.*, 369, 111
- Blain A. W., Chapman S. C., Smail I., Ivison R., 2004, *ApJ*, 611, 725
- Bolzonella M., Miralles J., Pelló R., 2000, *A&A*, 363, 476
- Borys C., Chapman S., Halpern M., Scott D., 2003, *MNRAS*, 344, 385

- Borys C., Smail I., Chapman S. C., Blain A. W., Alexander D. M., Ivison R. J., 2005, *ApJ*, 635, 853
- Boselli A., Lequeux J., Gavazzi G., 2002, *A&A*, 384, 33
- Bothwell M. S. et al., 2010, *MNRAS*, 405, 219
- Bouwens R. J. et al., 2009, *ApJ*, 705, 936
- Brunner H., Cappelluti N., Hasinger G., Barcons X., Fabian A. C., Mainieri V., Szokoly G., 2008, *A&A*, 479, 283
- Bruzual G., Charlot S., 2003, *MNRAS*, 344, 1000
- Bussmann R. S. et al., 2009, *ApJ*, 705, 184
- Calzetti D., Kinney A. L., Storchi-Bergmann T., 1994, *ApJ*, 429, 582
- Carilli C. L. et al., 2010, *ApJ*, 714, 1407
- Casey C. M. et al., 2009a, *MNRAS*, 399, 121
- Casey C. M. et al., 2009b, *MNRAS*, 395, 1249
- Casey C., Chapman S., Smail I., Alaghband-Zadeh S., Bothwell M., Swinbank A., 2011, *MNRAS*, 411, 2739
- Chapman S. C. et al., 2003, *ApJ*, 585, 57
- Chapman S. C., Smail I., Blain A. W., Ivison R. J., 2004, *ApJ*, 614, 671
- Chapman S. C., Smail I., Windhorst R., Muxlow T., Ivison R. J., 2004, *ApJ*, 611, 732
- Chapman S. C., Blain A. W., Smail I., Ivison R. J., 2005, *ApJ*, 622, 772
- Chapman S. C. et al., 2008, *ApJ*, 689, 889
- Clements D. L., Sutherland W. J., McMahon R. G., Saunders W., 1996, *MNRAS*, 279, 477
- Condon J. J., 1992, *ARA&A*, 30, 575
- Coppin K. et al., 2006, *MNRAS*, 372, 1621
- Coppin K. E. K. et al., 2007, *ApJ*, 665, 936
- Coppin K. E. K. et al., 2008, *MNRAS*, 389, 45
- da Cunha E., Charmandaris V., Diaz-Santos T., Armus L., Marshall J. A., Elbaz D., 2010, *A&A*, 523, 1487
- Daddi E., Cimatti A., Renzini A., Fontana A., Mignoli M., Pozzetti L., Tozzi P., Zamorani G., 2004, *ApJ*, 617, 746
- Daddi E. et al., 2007, *ApJ*, 670, 173
- Daddi E., Dannerbauer H., Elbaz D., Dickinson M., Morrison G., Stern D., Ravindranath S., 2008, *ApJ*, 673, L21
- Daddi E. et al., 2010, *ApJ*, 713, 686
- Danielson A. L. R. et al., 2010, *MNRAS*, 1565
- Dannerbauer H., Daddi E., Riechers D. A., Walter F., Carilli C. L., Dickinson M., Elbaz D., Morrison G. E., 2009, *ApJ*, 698, L178
- Dasyra K. M. et al., 2006, *ApJ*, 638, 745
- Davé R., Finlator K., Oppenheimer B. D., Fardal M., Katz N., Kereš D., Weinberg D. H., 2010, *MNRAS*, 404, 1355
- Dekel A. et al., 2009, *Nat*, 457, 451
- Dey A. et al., 2008, *ApJ*, 677, 943
- Dib S., Bell E., Burkert A., 2006, *ApJ*, 638, 797
- Dowell C. D. et al., 2003, in Phillips T. G., Zmuidzinas J., eds, *Proc. SPIE*, 4855, 73
- Downes D., Solomon P. M., 1998, *ApJ*, 507, 615
- Eales S., Lilly S., Webb T., Dunne L., Gear W., Clements D., Yun M., 2000, *AJ*, 120, 2244
- Elmegreen B. G., 1999, *ApJ*, 517, 103
- Engel H. et al., 2010, *ApJ*, 724, 233
- Erb D. K., Steidel C. C., Shapley A. E., Pettini M., Reddy N. A., Adelberger K. L., 2006, *ApJ*, 647, 128
- Fan X. et al., 2001, *AJ*, 121, 54
- Fixsen D. J., Bennett C. L., Mather J. C., 1999, *ApJ*, 526, 207
- Fomalont E. B., Kellermann K. I., Cowie L. L., Capak P., Barger A. J., Partridge R. B., Windhorst R. A., Richards E. A., 2006, *ApJS*, 167, 103
- Frayser D. T. et al., 1999, *ApJ*, 514, L13
- Gao Y., Solomon P. M., 2004, *ApJ*, 606, 271
- Genzel R., Baker A. J., Tacconi L. J., Lutz D., Cox P., Guilloteau S., Omont A., 2003, *ApJ*, 584, 633
- Genzel R. et al., 2008, *ApJ*, 687, 59
- Goto T. et al., 2010, *A&A*, 514, A6+
- Greve T. R. et al., 2005, *MNRAS*, 359, 1165
- Greve T. R., Pope A., Scott D., Ivison R. J., Borys C., Conselice C. J., Bertoldi F., 2008, *MNRAS*, 389, 1489
- Hainline L. J., Blain A. W., Greve T. R., Chapman S. C., Smail I., Ivison R. J., 2006, *ApJ*, 650, 614
- Hainline L. J., Blain A. W., Smail I., Frayer D. T., Chapman S. C., Ivison R. J., Alexander D. M., 2009, *ApJ*, 699, 1610
- Helou G., Soifer B. T., Rowan-Robinson M., 1985, *ApJ*, 298, L7
- Hinshaw G. et al., 2009, *ApJS*, 180, 225
- Ivison R. J. et al., 2002, *MNRAS*, 337, 1
- Ivison R. J. et al., 2007, *ApJ*, 660, L77
- Ivison R. J. et al., 2010a, *MNRAS*, 402, 245
- Ivison R. J. et al., 2010b, *A&A*, 518, L31
- Ivison R. J. et al., 2011, *MNRAS*, 412, 1913
- Kennicutt R. C., Jr, 1998, *ApJ*, 498, 541
- Kovács A., Chapman S. C., Dowell C. D., Blain A. W., Ivison R. J., Smail I., Phillips T. G., 2006, *ApJ*, 650, 592
- Lawrence A., Rowan-Robinson M., Leech K., Jones D. H. P., Wall J. V., 1989, *MNRAS*, 240, 329
- Melnick J., Mirabel I. F., 1990, *A&A*, 231, L19
- Menéndez-Delmestre K. et al., 2009, *ApJ*, 699, 667
- Miyazaki S. et al., 2002, *PASJ*, 54, 833
- Monaco P., 2004, *MNRAS*, 352, 181
- Morrison G. et al., 2008, in Chary R.-R., Teplitz H. I., Sheth K., eds, *ASP Conf. Ser. Vol. 381, Infrared Diagnostics of Galaxy Evolution*. Astron. Soc. Pac., San Francisco, p. 376
- Mushotzky R. F., Cowie L. L., Barger A. J., Arnaud K. A., 2000, *Nat*, 404, 459
- Muxlow T. W. B. et al., 2005, *MNRAS*, 358, 1159
- Narayanan D., Cox T. J., Hayward C. C., Younger J. D., Hernquist L., 2009, *MNRAS*, 400, 1919
- Neri R. et al., 2003, *ApJ*, 597, L113
- Noeske K. G. et al., 2007, *ApJ*, 660, L43
- Pope A. et al., 2006, *MNRAS*, 370, 1185
- Pope A. et al., 2008, *ApJ*, 689, 127
- Reddy N. A., Steidel C. C., Erb D. K., Shapley A. E., Pettini M., 2006, *ApJ*, 653, 1004
- Reddy N. A., Steidel C. C., Pettini M., Adelberger K. L., Shapley A. E., Erb D. K., Dickinson M., 2008, *ApJS*, 175, 48
- Richards E. A., 2000, *ApJ*, 533, 611
- Richards G. T. et al., 2006, *AJ*, 131, 2766
- Riechers D. A. et al., 2006, *ApJ*, 650, 604
- Sanders D. B., Mirabel I. F., 1996, *ARA&A*, 34, 749
- Sanders D. B., Soifer B. T., Elias J. H., Madore B. F., Matthews K., Neugebauer G., Scoville N. Z., 1988, *ApJ*, 325, 74
- Scoville N. Z., Yun M. S., Brown R. L., Vanden Bout P. A., 1995, *ApJ*, 449, L109
- Solomon P. M., Downes D., Radford S. J. E., Barrett J. W., 1997, *ApJ*, 478, 144
- Steidel C. C., Shapley A. E., Pettini M., Adelberger K. L., Erb D. K., Reddy N. A., Hunt M. P., 2004, *ApJ*, 604, 534
- Swinbank A. M. et al., 2008, *MNRAS*, 391, 420
- Tacconi L. J. et al., 2006, *ApJ*, 640, 228
- Tacconi L. J. et al., 2008, *ApJ*, 680, 246
- Tacconi L. J. et al., 2010, *Nat*, 463, 781
- Thomasson P., 1986, *QJRAS*, 27, 413
- Thompson T. A., Quataert E., Murray N., 2005, *ApJ*, 630, 167
- Ueda Y. et al., 2008, *ApJS*, 179, 124
- Veilleux S. et al., 2009, *ApJS*, 182, 628
- Weingartner J. C., Draine B. T., 2001, *ApJ*, 548, 296
- Weiss A., Downes D., Walter F., Henkel C., 2007, in Baker A. J., Glenn J., Harris A. I., Mangum J. G., Yun M. S., eds, *ASP Conf. Ser. Vol. 375, From Z-Machines to ALMA: (Sub)Millimeter Spectroscopy of Galaxies*. Astron. Soc. Pac., San Francisco, p. 25
- Weiß A., Downes D., Neri R., Walter F., Henkel C., Wilner D. J., Wagg J., Wiklind T., 2007, *A&A*, 467, 955
- Wiebe D. V. et al., 2009, *ApJ*, 707, 1809
- Yun M. S., Reddy N. A., Condon J. J., 2001, *ApJ*, 554, 803

This paper has been typeset from a $\text{\TeX}/\text{\LaTeX}$ file prepared by the author.